frontiers | Frontiers in Remote Sensing

TYPE Original Research
PUBLISHED 04 August 2025
DOI 10.3389/frsen.2025.1624783

OPEN ACCESS

EDITED BY
Sawaid Abbas,
University of the Punjab, Pakistan

REVIEWED BY
Lewis McCaffrey,
State of New York, United States
Changpeng Li,
Ministry of Natural Resources, China
Alba German,
Instituto de Altos Estudios Espaciales Mario Gulich, Argentina

*CORRESPONDENCE
Akash Ashapure,
akash.ashapure@nasa.gov

RECEIVED 07 May 2025
ACCEPTED 15 July 2025
PUBLISHED 04 August 2025

CITATION
Kabir S, Saranathan AM, Barnes BB, Ashapure A, O'Shea RE and Stengel VG (2025) Feasibility of PlanetScope SuperDove constellation for water quality monitoring of inland and coastal waters. *Front. Remote Sens.* 6:1624783. doi: 10.3389/frsen.2025.1624783

Feasibility of PlanetScope SuperDove constellation for water quality monitoring of inland and coastal waters

Sakib Kabir[1], Arun M. Saranathan[1,2], Brian B. Barnes[3], Akash Ashapure[1,2]*, Ryan E. O'Shea[1,2] and Victoria G. Stengel[4]

[1]Science Systems and Applications, Inc, Lanham, MD, United States, [2]NASA Goddard Space Flight Center, Greenbelt, MD, United States, [3]University of South Florida, StPetersburg, FL, United States, [4]U.S. Geological Survey Geology, Energy and Minerals Science Center, Reston, VA, United States

Planet's SuperDove (SD) sensors offer eight bands (seven visible, one near infrared (NIR)) at 3 m spatial and near-daily temporal resolution. The yellow (610 nm) and red-edge (705 nm) bands are valuable for retrieving water quality (WQ) parameters, supporting applications such as harmful algal bloom (HAB) and post-disaster monitoring. To enable scientific use, we assess signal-to-noise ratios (SNRs), with the highest (248:1) at 443 nm and the lowest (8:1) at 865 nm, and other visible bands ranging from 26:1–98:1. We cross-calibrated SD with Sentinel-2 Multi-Spectral Imager (MSI) using near-simultaneous observations over aquatic environments by comparing top-of-atmosphere (TOA; ρ_t) reflectance across five shared visible bands (443, 490, 565, 665, and 705 nm), and derived calibration coefficients through linear regression. Before calibration, SD-MSI median ρ_t differences ranged from ~0.7–13%, with highest differences at 705 nm. After applying the calibration, these differences reduced to −0.07% to −2.2%, including improvements at 665 nm (from ~8% to −2.2%) and 705 nm (from ~13% to −0.1%). Differences in atmospherically corrected remote sensing reflectance (R_{rs}) also decreased from 16%–95% to 8%–72% post-calibration, with 565 nm showing the lowest (~8%) and 705 nm the highest (~72%) residual difference. Remaining R_{rs} discrepancies are attributed in part to SD's inter-sensor differences and uncertainties in atmospheric correction. We qualitatively compared chlorophyll-a (Chla) and Secchi-disk depth (Z_{sd}) WQ products from SD and MSI, including a time-series analysis focused on the Dixie Fire and subsequent algal bloom in Lake Almanor (Sept–December 2021). The products captured expected trends, highlighting SD's potential for WQ monitoring, while elevated uncertainties in ρ_t and R_{rs} suggest the need for improved calibration stability and atmospheric correction.

KEYWORDS

superdove, radiometry, signal-to-noise ratio, top-of-atmosphere (TOA) reflectance, remote sensing reflectance, inland/coastal waters, water quality

1 Introduction

Government-supported missions, such as Landsat 8/9 (L8/L9) and Sentinel-2 A/B (S2) multispectral imager (MSI), provide decameter scale (10–60 m) optical images at 8- or 5-day revisit rates (Li and Chen, 2020). Even though these sensors were designed for terrestrial science and applications, high-quality (i.e., with high levels of radiometric, spatial, and

TABLE 1 SuperDove's (SD) spectral bands, wavelengths, full-width half maximum (FWHM), ground sampling distance (GSD) and spatial sampling.

Band number	Band name	Wavelength (FWHM)[(nm]	GSD [m]	Spatial sampling
1	Coastal blue	443 (20)	12	0.25x
2	Blue	490 (50)	3	1x
3	Green I	531 (36)	3	1x
4	Green II	565 (36)	3	1x
5	Red	665 (31)	3	1x
6	Yellow	610 (20)	6	0.5x
7	Red edge	705 (15)	6	0.5x
8	NIR	865 (40)	6	0.5x

spectral resolution) observations (Kabir et al., 2023; Pahlevan et al., 2017a; Pahlevan et al., 2019; 2014) and improved atmospheric correction (AC) processors (Pahlevan et al., 2021; Wang et al., 2019; Warren et al., 2019; Wei et al., 2018) permit their usage to monitor and study aquatic ecosystems. More specifically, images from these missions have been used to retrieve chlorophyll-a (Chl*a*) concentration (Cao et al., 2022), total suspended solids (TSS) (Balasubramanian et al., 2020), water turbidity (Kuhn et al., 2019; Vanhellemont and Ruddick, 2014), water transparency or Secchi-disk depth (Z_{sd}) (Lee et al., 2016), bathymetry (Caballero and Stumpf, 2019; Pacheco et al., 2015), *etc.* Commercial satellite missions (*e.g.,* PlanetScope, WorldView, *etc.*) with meter scale optical imagers (<10 m) and high revisit rate (near daily) have spurred similar water-related applications (Lewis et al., 2023; Pitarch and Vanhellemont, 2021; Vanhellemont, 2019a; Vanhellemont and Ruddick, 2018).

Planet Labs PlanetScope satellite-born sensors have been collecting images for over a decade, which commenced with Dove-classic, followed by Dove-R and SuperDove (SD) sensors in 2017, 2018 and 2019, respectively. Dove-classic and -R were launched with the capability of collecting four spectral bands, whereas SD sensors were equipped with four additional bands. An eight-band SD image is generated by stacking together several consecutive frames on either side of a given frame using Structure-from-Motion, where each frame consists of eight stripes (Jumpasut et al., 2020). An SD image covers approximately 32.5 km by 19.6 km area, and the images are collected with 12-bit radiometric resolution. Table 1 shows the spectral bands, full-width half maximum (FWHM), ground sampling distance (GSD), and spatial sampling of SD instruments (Fernandez-Saldivar et al., 2020). SD instruments were first launched in April 2019 and were replenished frequently to collect eight band images at high spatial (~3 m) and temporal resolutions (~daily). SD's yellow (610 nm) and red-edge (705 nm) bands are aligned closely in the proximity of spectral signatures critical in monitoring cyanobacteria blooms (cyanoHABs), making them a viable option for aquatic science and applications. A few water-related studies demonstrated the potential of SD sensors for Chl*a* concentration retrieval (Vanhellemont, 2023), bathymetry (Niroumand-Jadidi et al., 2022), and sediment mapping (Zhang et al., 2023).

To exploit the SD observations more effectively, the quality (radiometric, spatial, spectral, and geometric) of the observations must be assessed and improved (Gordon, 1987; IOCCG, 2012; Kabir et al., 2020; Roy et al., 2017). Radiometric quality of SD observations is assessed and improved using vicarious techniques due to the lack of onboard calibrating instruments (*e.g.,* shutter, lamp, solar diffuser). In practice, SD sensors are calibrated over terrestrial sites, every 6 months (January 1st and July 1st) using near-simultaneous observations with S2/MSI and validated with Radiometric Calibration Network (RadCalNet) (Collison et al., 2021). SD's absolute/relative radiometric performance is evaluated occasionally. For instance, Saunier and Cocevar (2022, pg. 52) reported 0.4%–6.7% top-of-atmosphere (TOA) reflectance (ρ_t) difference with MSI for two SD-MSI crossovers in Libya (Saunier and Cocevar, 2022) and 0.5%–2.2% difference with one of the RadCalNet sites in La Crau, France, where one SD observation was assessed. A system characterization report from the U.S. Geological Survey (USGS) presented a 4%–11% difference between two SD and MSI ρ_t observations (USGS, 2020). Recently, in 2024, Lavender, (2024) presented about -15%–10% ρ_t differences in four bands (443, 565, 665 and 865 nm) of SD (five different sensors) with two RadCalNet sites in La Crau, France and Gobabeb, Namibia. These varying degrees of performance indicate that the radiometry (calibration, noise, stability, *etc.*) of SD should be assessed and improved, as suggested by Frazier and Hemingway, (2021). For aquatic science and applications, radiometric performance of SD sensors should be evaluated over bodies of water and improved, as these instruments may exhibit different radiometric responses compared to well-calibrated sensors, such as S2/MSI, L8/L9.

Firstly, this work presents the signal-to-noise ratio (SNR) assessment of SD bands over aquatic environments, which allows evaluation of the noise characteristics of SD images. This work further aimed to cross-calibrate SD sensors with S2/MSI using near-simultaneous observations over aquatic ecosystems. Here, S2/MSI was exploited as a reference sensor to cross-calibrate and improve the SD constellation due to their nearly overlapping spectral bands (five bands) (Tu et al., 2022). Specifically, we aimed to cross-compare the SD sensors' ρ_t product to MSI ρ_t over bodies of water and derive calibration coefficients (gains and offsets) to align the SD imagery more closely with the radiometric properties of MSI. Then, we evaluate the performance of SD ρ_t against MSI ρ_t with an independent dataset after updating the SD ρ_t with the newly derived calibration coefficients. One of the most

critical components for aquatic applications of remotely sensed optical images is the AC processor (Wang, 2010). We evaluate the ACOLITE AC processor generated (Vanhellemont, 2023; 2019b) remote sensing reflectance (R_{rs}) product of SD with MSI. Finally, to demonstrate the feasibility of improved SD observations, we developed WQ parameter retrieval model to map Chl*a* and Z_{sd}, and presented visual assessment of the WQ product over a few select locations and a time-series analysis for one episodic event.

This manuscript is structured as follows. Section 2 presents materials and methods which elaborate on the dataset, SNR assessment techniques, ρ_t cross-calibration and validation methods, R_{rs} assessment techniques, WQ parameter retrieval model, and the performance metrices. SNR assessment, cross-calibration, and validation of ρ_t, R_{rs} assessment, and WQ product retrieval results are summarized in Section 3. Section 4 provides discussions and future directions, and the final section (Section 5) presents a summary and conclusions.

2 Materials and methods

This section a) presents the dataset used for cross-calibration and validation (Section 2.1), b) explains SNR analysis technique (Section 2.2), c) describes cross-calibration and validation methods (Section 2.3), d) delineates R_{rs} product assessment approach (Section 2.4), e) describes water quality products retrieval method (Section 2.5), and f) presents performance metrics (Section 2.6).

2.1 Dataset

Near-simultaneous SD-MSI observations, collected within 10 min, were searched globally over water bodies exploiting Planet Labs (hereafter Planet) application programming interface (API) (https://docs.planet.com/data/) and European Space Agencies (ESA) Copernicus Data Space Ecosystem (CDSE) API ((https://dataspace.copernicus.eu/). Access to the Planet's API was provided under NASA's Commercial Smallsat Data Acquisition (CSDA) program (NASA Earth Science Division, 2020), and ESA CDSE API was openly available. Firstly, SD-MSI image pairs were searched and identified from July 2023 to December 2023, and they are referred to as "calibration data." This time frame was selected to align with Planet's calibration cycle and to ensure consistent sensor behavior following routine quarterly updates and maintenance, as recommended in Planet's guidelines (Collison et al., 2021). Then SD-MSI image pairs, collected from January 2024 to May 2024, were searched, and they are referred to as "validation data". PlanetScope SD orthorectified images were downloaded from Planet's API and S2/MSI L1C products were downloaded from CSDE API. Each downloaded SD orthorectified image consists of a scaled TOA radiance file, a metadata file, and a usable data mask (UDM2) file (Team, 2023).

2.2 Signal-to-noise ratio assessments

To investigate the random and/or systematic noises in the SD observations, SNRs of SD images were estimated from ρ_t (converted from scaled TOA radiance) for all eight bands. We selected seven cloud- and snow-free SD images from six different SD instruments over the clear waters of Crater Lake in Oregon, where solar zenith angles (SZA) were from 49° to 62°, and solar azimuth angles (SAA) varied from 119° to 148°. SD scene IDs used for SNR analysis can be found in Supplementary Appendix A (Supplementary Table SA.1). From an SD image, spatially uninform and clear water regions (>10,000 pixels) were manually identified by examining the ρ_t images, where there are no image artifacts. SNRs were computed by averaging the locally calculated mean (μ) to standard deviation (σ) ratio (i.e., μ/σ) from the seven images. The local mean and standard deviation were computed by applying a running 3 × 3 element window since larger window sizes (e.g., 5 × 5, 7 × 7, *etc.*) increase inter-pixel heterogeneity, amplifying random noise in the analysis (Hu et al., 2012).

2.3 Cross-calibration and validation

SD sensors were cross-calibrated and validated with MSI observations collected over global water bodies within 10 min of one another. Best practices were followed for identifying ideal matchup sites such that the difference between the observations is primarily due to their absolute radiometry. This cross-calibration was performed for the five common bands of SD and MSI (coastal blue (443 nm), blue (490 nm), green (565 nm), red (665 nm), and red-edge (705 nm)). The cross-calibration and validation was performed individually for each band. Note that SD TOA reflectance observations are operationally calibrated with MSI as a reference, suggesting that the SD and MSI observations should be directly comparable (Collison et al., 2021); hence, no spectral band adjustment has been performed throughout this study. Note also that the relative spectral response (RSR) of SD and MSI is nearly identical (Tu et al., 2022), and RSR-related differences are assumed to be negligible.

The procedure to identify suitable regions of interests (ROIs) to cross-calibrate and validate SD observations with MSI observations was as follows.

1. Convert SD and MSI observations to ρ_t. SD's scaled TOA radiances were converted to ρ_t by applying band-specific reflectance conversion factors provided in the metadata file. MSI digital numbers (DNs) were converted to ρ_t by applying offsets (applicable to the MSI data collected after 25th January 2022) and band-specific conversion factors (S. M. E. Team, 2022).
2. Mask SD and MSI images. SD images were masked for cloud, cloud shadow, and haze using the provided UDM2 mask (Team, 2023). SD and MSI images were further filtered for clouds, cloud shadows, sun glint, and land pixels using ACOLITE AC processor-generated L2 flags (Vanhellemont, 2023; 2019b).
3. Generate per-pixel MSI angle files for each band. Per-pixel viewing zenith angles (VZA) viewing azimuth angles (VAA), SZA, and SAA were generated for each MSI band following the procedure presented in Pahlevan et al. (2017b). Note that SD images come with a single image center VZA, VAA, SZA, and SAA for each image.
4. Identify ideal matchups in the SD and MSI image pairs. Ideal matchups were defined as regions where differences in the angles (VZA, VAA) are minimal. To eliminate extreme off-

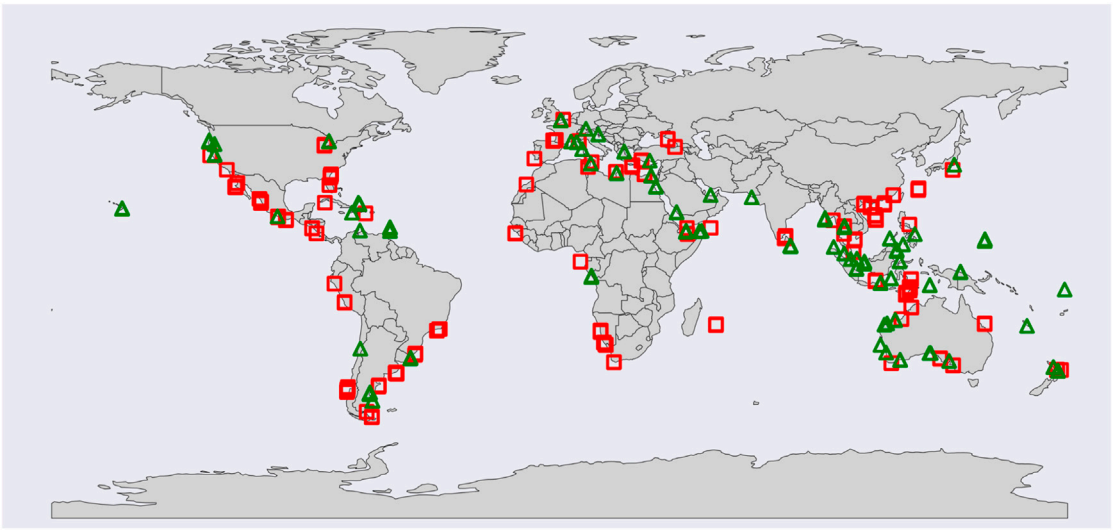

FIGURE 1
SuperDove (SD) - Multispectral Imager (MSI) near-simultaneous image pairs, including only the intercomparison regions that passed all the exclusion criteria. Red squares denote the 188-cross-calibration SD data and green triangles show the 119-validation SD data (not drawn to scale). The cross-calibration and validation datasets were distributed over different water bodies, including inland, coastal, and open oceans. Background map is obtained from Python's 'geopandas mapping and plotting tools' library (https://geopandas.org/en/v0.9.0/docs/user_guide/mapping.html).

nadir matchups, we discarded SD images and MSI pixels where VZA is $>5°$. Further, matchups with VZA differences ($\Delta VZA = VZA_{MSI} - VZA_{SD}$) larger than $\pm 3°$ were eliminated to minimize any angular effects in our analysis. We have also computed the related azimuth angle (RAA) for each MSI pixel and each SD image following the equation presented in Kabir et al. (2023), and discarded all the matchups where the RAA difference ($\Delta RAA = RAA_{MSI} - RAA_{SD}$) was larger than 100°. Note that any further constraints on the VZA, ΔVZA and ΔRAA thresholds did not yield an adequate number of matchups for analysis.

5. Locate homogenous ROIs in the MSI image. We calculated SNR within 7x7-element windows (all the pixels were valid) in MSI ρ_t images, by taking the ratio of mean and standard deviation for the visible bands. For aquatic applications, previously estimated (Pahlevan et al., 2017a) minimum SNR thresholds (443 nm: 439; 490 nm: 102; 565 nm: 79; 665 nm: 45; 705 nm: 45) were applied to identify matchup sites.
6. Eliminate the outer-edge pixels from each 7 × 7 (square) window of MSI. SD's absolute geolocation accuracy is ~14 m, which means the SD pixel offset could be ~five pixels (Semple et al., 2023). Moreover, signals originating from neighboring inhomogeneous pixels (i.e., edge pixel effect) and spatial resolution mismatches can reduce data consistency. To mitigate these impacts, two outer-edge pixels from the 7 × 7 square window were discarded and noted coordinates were used to calculate the average ρ_t of MSI and SD within the remaining 3x3-element window.
7. Discard inhomogeneous matchup sites. The spatial homogeneity in MSI and SD ρ_t was investigated by evaluating the coefficient of variations (CV) of each band. Specifically, matchup sites with $CV_{\rho_{t,SD}}(443) > 0.02$, $CV_{\rho_{t,SD}}(490, 565) > 0.01$, $CV_{\rho_{t,SD}}(665) > 0.06$ and $CV_{\rho_{t,SD}}(705) > 0.1$ were ignored. These thresholds were determined experimentally by assessing the distribution of SD ρ_t, CV, and the ratio of the average MSI and SD ρ_t of each matchup site for each band in a similar manner (Barnes et al., 2021; Kabir et al., 2023; Pahlevan et al., 2017b). Note again that this analysis was performed band-by-band, meaning that ideal matchup in one ROI for one band (e.g., 443 nm) might not be an ideal matchup for other bands (e.g., 490nm, 565 nm, *etc.*) in that ROI.

The above-explained matchup selection criteria were applied to the original full set of potential calibration (~4000 SD images) and validation (~2500 SD images) data. Following this screening process, 188 calibration SD images (60 MSI images) and 119 validation SD images (40 MSI images) remained to obtain cross-calibration parameters and validate the analysis, respectively. Figure 1 presents the global distribution of the calibration SD images (red squares) and validation SD images (green triangles), which includes different types of water bodies. Approximately 80% of the selected matchups are distributed across coastal regions, with the remaining 10% each covering inland and open ocean waters. This distribution reflects the greater availability of near-simultaneous SD-MSI observations over coastal areas, likely due to their proximity to land, higher revisit frequency, and increased likelihood of cloud-free scenes. The SNR estimation and calibration procedures exhibited linear computational complexity.

2.4 Remote sensing reflectance (R_{rs}) product assessment

The remote sensing reflectance (R_{rs}) is the ratio of water-leaving radiance to the total downwelling irradiance just above

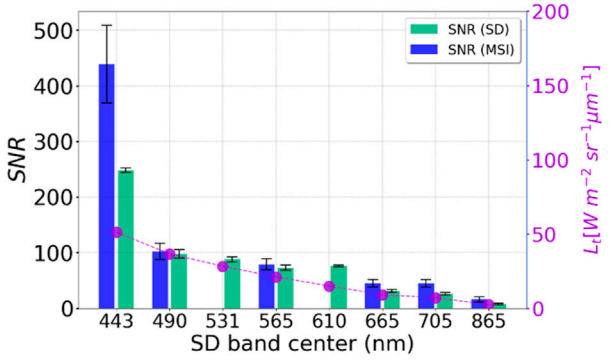

FIGURE 2
Bar graph comparing the signal-to-noise ratio (SNR) of multispectral imager (MSI) and SuperDove (SD) across various SD band centers in nanometers. SD SNRs estimated from seven SD images originating from six different SD instruments over Crater Lake in Oregon. The SNR for MSI is depicted in blue bars, while SD is shown in green bars. The SNR values generally decrease as the wavelength increases from 443 to 865 nm. A magenta line with circles indicates spectral radiance (Lt) along the right y-axis. Error bars are present for both SD and MSI readings.

the water surface (Mobley, 1999). The R_{rs} is retrieved from the ρ_t observations through AC. Successful mapping of water quality indicators (e.g., phytoplankton, the absorption by the colored dissolved organic matter (a_{cdom}), suspended particulate matter (SPM)) requires highly accurate R_{rs} products, which could be quite challenging due to the low magnitude of spectral R_{rs} relative to the interfering atmospheric contributions (Wang, 2010). Over the years, several AC methods (e.g., SeaDAS (Pahlevan et al., 2019), ACOLITE (Vanhellemont, 2019b), POLYMER (Steinmetz and Ramon, 2018), and the image correction for atmospheric effects (iCor) (De Keukelaere et al., 2018)) have been developed for different remote sensing satellites, and they demonstrated varying degrees of performance over different aquatic and atmospheric conditions (Pahlevan et al., 2021). As of this writing, only ACOLITE AC processor has been adopted for processing SD observations (Vanhellemont, 2023). An automated processing system based on SeaDAS is being developed at the Naval Research Laboratory, but this is not openly available (McCarthy et al., 2023). In this demonstration, the ACOLITE dark spectrum fitting (DSF) algorithm was used to process both SD and MSI observations for evaluating the performance of SD R_{rs} against MSI R_{rs}. For SD processing, the DSF algorithm assumes homogenous aerosol conditions over 3 × 3 km sub-images and estimates the aerosol optical depth from a constructed dark spectrum. In this study, ACOLITE version 20220222.0 was used for correcting SD and MSI observations. Validation of "as-is" SD ρ_t data and calibrated SD ρ_t data (using the cross-calibration coefficients derived in this study) were both processed through ACOLITE to generate R_{rs} products for each SD band, as well as the corresponding MSI R_{rs} products. These images allowed assessment of the performance of SD R_{rs} against the MSI R_{rs} products before and after the SD ρ_t calibration.

2.5 Water quality products

To demonstrate the value of these SD observations for WQ monitoring, particularly when combined with other satellite-based observations, we employed a machine learning (ML)-based mixture density network estimator (Pahlevan et al., 2022) to compare WQ indicators, such as Z_{sd} and Chl*a*, derived from SD (both before and after calibration) with corresponding estimates from near-simultaneous MSI observations. Traditional machine learning (ML) models assume that input variables are causal factors that determine the behavior of the output or observed variable. In cases where there is a well-defined relationship between inputs and outputs, ML models learn this relationship using a set of known input-output pairs, or training samples. This scenario, known as *forward modeling*, ensures that the output distribution (as a function of the input) is unimodal, i.e., the input-output mapping is either one-to-one or many-to-one. However, estimating Water Quality Indicators (WQI) from remote sensing reflectance (R_{rs}) is an *inverse problem*, wherein we attempt to infer causal factors of watercolor (such as Chla and Z_{sd}) from the dependent variable , R_{rs}. Inverse problems often involve a multimodal output distribution, due to a *one-to-many mapping*, making them challenging for traditional ML approaches. Mixture Density Networks (MDNs) (Bishop, 1994) address this challenge by modeling the output variable as a mixture of Gaussian distributions, allowing them to capture multimodal output distributions effectively. MDN models have shown promising results to map these nonunique relationships and retrieve WQ parameters such as Chl*a*, TSS, Z_{sd} and a_{cdom} from multispectral observations from the following satellite/sensor combinations: L8/OLI, S2/MSI, Sentinel-3's Ocean and Land Color Instrument (OLCI), the Moderate Resolution Imaging Spectroradiometer (MODIS), and the Visible Infrared Imaging Radiometer Suite (VIIRS) (Balasubramanian et al., 2025; 2020; Fickas et al., 2023; Maciel et al., 2023; Pahlevan et al., 2020; Smith et al., 2021). In this study, we developed MDNs for retrieving Chl*a* and Z_{sd} from SD and MSI images. The MDNs implementation details are provided in Supplementary Appendix C. Note that, here, we showcase the relative retrieval quality from SD images and demonstrate their efficacy for aquatic applications.

2.6 Performance metrics

SD observations were cross-calibrated with MSI data using ordinary least square linear regression (OLSLR) for the five SD-MSI bands. Slopes and intercepts from the OLSLR fit are the calibration gains and offsets, which are referred to as "calibration parameters". To evaluate the agreements/discrepancies between SD-MSI before and after applying calibration parameters, the following metrics were also computed.

Differences in the MSI and SD products are expressed as percentage differences ($PD_{\lambda i}$), and root-mean-squared difference ($RMSD_{\lambda i}$). $PD_{\lambda i}$ is defined as follows:

$$PD_{\lambda i} = \left[\left(\chi^{SD(\lambda i)} - \chi^{MSI(\lambda i)}\right)\Big/\chi^{MSI(\lambda i)}\right] \times 100$$

where χ is the Level 1 (ρ_t) or Level 2 (R_{rs}) reflectance product for band λ_i. Note that λi is dropped for brevity in the following sections.

TABLE 2 SuperDove (SD) signal-to-noise ratios (SNRs) for the visible and near infrared (NIR) band.

Band [nm]	443	490	531	565	610	665	705	865
L_t	65	46	28	22	15	10	9	6
SNR	248	98	88	73	76	31	26	8

The median $PD_{\lambda i}$ is hereafter referred to as median percentage difference (MPD). Variability or dispersion in the $PD_{\lambda i}$ was calculated using median absolute deviation (MAD), which is defined as: $MAD_{\lambda i} = median(|PD_{\lambda i} - median(PD_{\lambda i})|)$.

RMSD and bias were computed as follows:

$$RMSD = \sqrt{\left(\frac{1}{N}\sum(\chi^{SD} - \chi^{MSI})^2\right)}$$

$$bias = \frac{1}{N}\sum(\chi^{SD} - \chi^{MSI})$$

where χ^{SD} and χ^{MSI} are the ρ_t or R_{rs} of SD and MSI, respectively. N denotes the number of matchups for each spectral band.

The median difference (MD) was also calculated as below:

$$MD = Median\ (\chi^{SD} - \chi^{MSI})$$

Due to the presence of noise in the analyses, the median metric was preferred over mean. The inter-consistency of MSI and SD products were gauged with these metrics, OLSLR statistics, including slope and intercept, and the coefficient of determination (R^2).

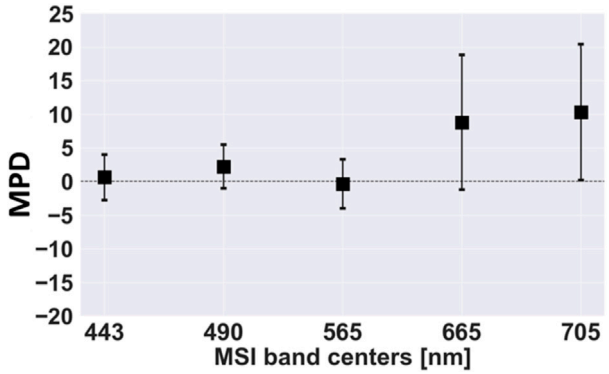

FIGURE 3
SuperDove (SD) and Multispectral Imager (MSI) top-of-atmosphere (TOA) reflectance (ρ_t) product inter-comparison for the visible and red-edge bands. The data points indicate the median percent difference (MPD) for the matchups in each spectral band for near-simultaneous observations. The error bars represent 1-σ standard deviation. Refer to Table 3 for more statistical descriptors and Supplementary Appendix B (Supplementary Figure SB1) for scatterplots.

3 Results

3.1 Signal-to-noise ratio assessments

SD SNRs computed from ρ_t are presented in Figure 2 along with the over water MSI SNRs reported in Pahlevan et al. (2017a). The bars show average SNR calculated from ρ_t, error bars denote one-σ standard deviation, and average TOA radiances (L_t) are presented in the secondary axis. SD SNRs and L_t for each band are also presented in Table 2. It is evident from Figure 2 and Table 2 that the 443 nm band exhibits the highest SNR of 248, whereas the other bands have SNR <100. SD's red (665 nm) band SNR was found to be 31 while two green (531 and 565 nm) band's SNRs were 88 and 73, respectively. SNRs of the red-edge (705 nm) and NIR (865 nm) band were 26 and 8, respectively. For all the presented bands, SD SNR was less than MSI SNR, indicating that the ρ_t and downstream products from the SD might contain more random/systematic noise than those of MSI.

3.2 Cross-calibration and validation

3.2.1 Cross-calibration

The SD-MSI differences in unitless ρ_t from the calibration dataset are presented in Figure 3, represented as MPD and associated one-σ standard deviation error bars. The cross-calibration statistics are provided in Table 3 and the scatterplots of the five investigated bands are illustrated in Supplementary Appendix B (Supplementary Figure SB1). The number of matchups (N), average MSI TOA reflectance ($\bar{\rho}_{t,MSI}$), standard deviation in MSI TOA reflectance ($\sigma_{\rho_{t,MSI}}$), slopes/gains, intercepts/offsets, R^2, RMSD, bias, MD, MPD, and MAD are presented in Table 3. Overall, the shorter wavelengths (443, 490 and 565 nm) exhibited lower SD-MSI differences than the 665 and 705 nm bands, and SD's radiometric response was higher than MSI bands, except for the 565 nm band. MPDs of ~2.2% or less were found for the 443, 490 and 565 nm bands. Among them, the lowest difference (~−0.35%) was observed in the green band (ρ_t(565)), whereas ρ_t(443) and ρ_t(490) agreed within ~0.7% and 2.2%, respectively. Differences in ρ_t(665) and ρ_t(705) were ~9% and 10%, respectively. Using these results, we sought to reduce the radiometric inconsistency between SD and MSI by applying calibration parameters (i.e., applying gains and offsets). In this study, slopes and intercepts, derived from the linear regression analysis, were the gains and offsets derived for each band.

3.2.2 Validation

The SD-MSI differences in ρ_t (from the validation data) are presented in Figure 4A. The statistical descriptors are provided in Table 4 and the scatterplots of the five investigated bands are illustrated in Supplementary Appendix B (Supplementary Figure SB2). Unsurprisingly, the ρ_t differences between SD and MSI were found to be very similar to the differences observed in the cross-calibration analysis (section 3.2.1). The highest discrepancy of ~13% was evident in ρ_t(705) while ρ_t(490) showed ~0.74% difference. SD's radiometric response was also higher for the four bands.

TABLE 3 The SuperDove (SD) - Multispectral Imager (MSI) top-of-atmosphere (TOA) reflectance (ρ_t) product inter-consistency metrices derived using least square regression on the calibration data. The unitless $\bar{\rho}_{t,MSI}$ and $\sigma_{\rho_{t,MSI}}$ represent the average MSI TOA reflectance for the matchups and standard deviation, respectively. Note that these slopes and intercepts are the calibration parameters used in the validation (Section 3.2.2).

Band [nm]	N	$\bar{\rho}_{t,MSI}$	$\sigma_{\rho_{t,MSI}}$	Slope	Intercept	R^2	RMSD	Bias	MD	MPD [%]	MAD [%]
443	166,255	0.162	0.022	0.9709	0.00736	0.971	5.9E-03	2.6E-03	1.1E-03	0.65	2.75
490	31,206	0.126	0.013	0.9882	0.00494	0.951	5.3E-03	3.4E-03	2.7E-03	2.24	2.88
565	65,558	0.109	0.024	0.9862	0.00161	0.986	4.0E-03	1.0E-04	−3.4E-04	−0.35	2.96
665	105,117	0.054	0.009	1.0643	0.00222	0.887	7.9E-03	5.7E-03	4.8E-03	8.81	8.77
705	98,572	0.045	0.011	0.9025	0.00873	0.940	5.9E-03	4.3E-03	4.5E-03	10.30	11.63

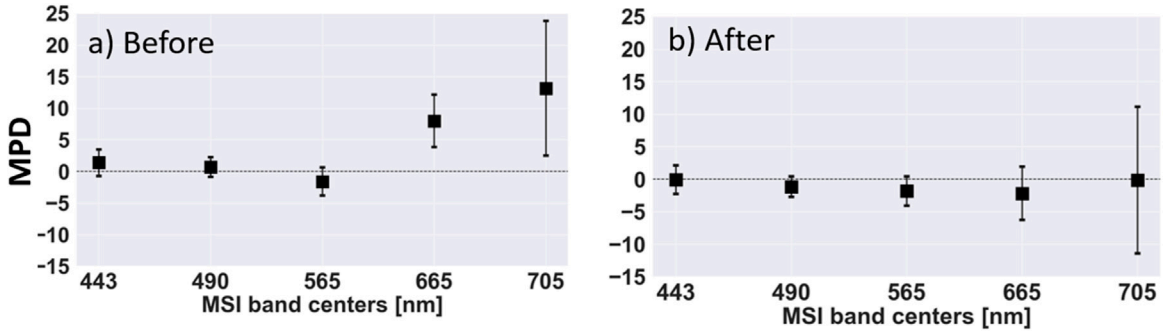

FIGURE 4
SuperDove (SD) and Multispectral Imager (MSI) top-of-atmosphere (TOA) reflectance (ρ_t) product inter-comparison for the visible bands: **(a)** before and **(b)** after applying cross-calibration parameters. The data points indicate median percentage differences (MPDs) for the matchups in each spectral band for near-simultaneous observations. The error bars represent 1-σ standard deviation. Refer to Tables 4 and 5 for more statistical descriptors, and Figures B2-B3 in Supplementary Material for scatterplots.

TABLE 4 The SuperDove (SD) – Multispectral Imager (MSI) top-of-atmosphere (TOA) reflectance (ρ_t) product inter-consistency metrics generated from near-simultaneous validation observations before applying calibration parameters.

Band [nm]	N	$\bar{\rho}_{t,MSI}$	$\sigma_{\rho_{t,MSI}}$	Slope	Intercept	R^2	RMSD	Bias	MD	MPD [%]	MAD [%]
443	5,994	0.162	0.014	1.0121	−0.00067	0.973	3.6E-03	1.3E-03	2.4E-03	1.39	2.18
490	16,266	0.163	0.021	0.9838	0.00366	0.995	2.3E-03	1.0E-03	1.2E-03	0.74	1.22
565	14,889	0.102	0.014	0.9577	0.00243	0.987	2.9E-03	−1.9E-03	−1.6E-03	−1.59	1.67
665	16,803	0.054	0.007	1.0639	0.00092	0.965	4.9E-03	4.4E-03	4.6E-03	8.01	3.75
705	16,654	0.040	0.006	0.9238	0.00866	0.803	6.9E-03	5.6E-03	4.8E-03	13.16	11.79

Calibration parameters (i.e., slopes/gains and intercepts/offsets) developed in section 3.2.1 (refer to Table 3) were then applied to the validation SD ρ_t observations. Figure 4B illustrates the SD-MSI ρ_t differences after applying calibration parameters, with the linear regression statistics presented in Table 5, and the scatterplots are illustrated in Supplementary Appendix B (Supplementary Figure SB3). From Figures 4A,B and Tables 4 and 5, it is apparent that the SD-MSI ρ_t differences had reduced substantially for a few bands (e.g., 665 and 705 nm) after applying calibration. Notably, for ρ_t(705), MPD decreased from ~13% to ~ −0.1%, RMSD reduced from ~0.0069 to ~0.0045, and bias reduced from ~0.0056 to ~0.00009. The red band (ρ_t(665)) also exhibited noticeable improvements, with MPDs reduced from ~8% to ~ −2.2%, RMSD decreased from 0.0049 to 0.0024, bias improved from 0.0044 to 0.001, and MD reduced from 0.00046 to −0.00012. The other three bands (443, 490 and 565 nm) did not show striking improvements, although ρ_t(443) exhibited a slight reduction in discrepancies, with similar RMSD and bias. Before and after calibration, ρ_t(490) and ρ_t(565) exhibited similar differences (<2% MPDs). Overall, after applying calibration SD-MSI ρ_t shows ~ −2.2% or less differences.

3.3 Remote sensing reflectance (R_{rs}) product assessment

The primary objective of this section is to evaluate the SD R_{rs} products retrieved using the ACOLITE AC processor before and

TABLE 5 The SuperDove (SD) - Multispectral Imager (MSI) top-of-atmosphere (TOA) reflectance (ρ_t) product inter-consistency metrics generated from near-simultaneous validation observations after applying calibration parameters.

Band [nm]	N	$\bar{\rho}_{t,MSI}$	$\sigma_{\rho_{t,MSI}}$	Slope	Intercept	R^2	RMSD	Bias	MD	MPD [%]	MAD [%]
443	5,994	0.162	0.014	1.0424	−0.00827	0.973	3.8E-03	−1.4E-03	−1.1E-04	−0.07	2.42
490	16,266	0.163	0.021	0.9955	−0.00130	0.995	2.9E-03	−2.0E-03	−1.8E-03	−1.14	0.99
565	14,889	0.102	0.014	0.9711	0.00083	0.987	3.1E-03	−2.1E-03	−1.9E-03	−1.82	1.72
665	16,803	0.054	0.007	0.9996	−0.00122	0.965	2.4E-03	1.0E-03	−1.2E-03	−2.17	3.57
705	16,654	0.040	0.006	1.0236	−0.00008	0.803	4.5E-03	0.9E-03	−5.8E-05	−0.14	13.22

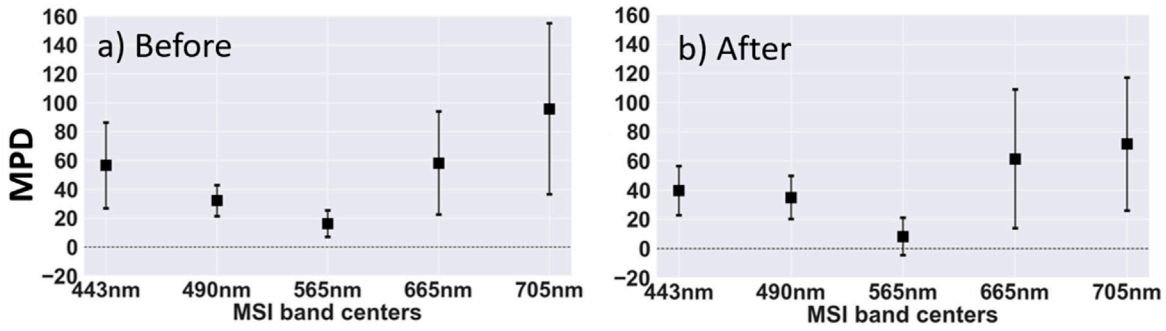

FIGURE 5
SD and MSI remote sensing reflectance (R_{rs}) product inter-comparison for the visible bands: **(a)** before, and **(b)** after applying calibration. The data points indicate the median percent difference (MPD) for the matchups in each spectral band for near-simultaneous observations. The error bars represent 1-σ standard deviation. Refer to Table 6 and 7 for more statistical descriptors.

TABLE 6 The SuperDove (SD) - Multispectral Imager (MSI) remote sensing reflectance (R_{rs}) product inter-consistency metrics generated from the near-simultaneous validation dataset (before calibration) using ACOLITE atmospheric correction (AC) processor. Note that the R_{rs} products are compared over the same matchup sites used for top-of-atmosphere (TOA) reflectance (ρ_t) validation. The $\bar{R}_{rs,MSI}$ and $\sigma_{R_{rs,MSI}}$ represents the average MSI R_{rs} for the matchups, and standard deviation, respectively.

Band [nm]	N	$\bar{R}_{rs,MSI}$	$\sigma_{R_{rs,MSI}}$	Slope	Intercept	R^2	RMSD	Bias	MD	MPD [%]	MAD [%]
443	5,994	0.009	0.004	0.8640	0.00726	0.870	6.3E-03	5.9E-03	6.7E-03	57	30
490	16,266	0.010	0.005	0.9149	0.00402	0.986	3.3E-03	3.1E-03	3.1E-03	32	11
565	14,889	0.012	0.003	0.8699	0.00368	0.948	2.2E-03	2.1E-03	1.9E-03	16	9
665	16,803	0.004	0.001	0.9247	0.00356	0.731	3.5E-03	3.2E-03	2.7E-03	58	36
705	16,654	0.003	0.001	1.2976	0.00233	0.769	3.7E-03	3.3E-03	3.4E-03	95	60

after applying cross-calibration parameters to ρ_t. Quantitative R_{rs} assessment over the validation matchup sites is presented in Section 3.3.1, and qualitative R_{rs} comparison (over a few select sites) is provided in Section 3.3.2.

3.3.1 Quantitative remote sensing reflectance (R_{rs}) assessment

The MPD in SD-MSI R_{rs} products (from the validation data) are illustrated in Figure 5A. The one-to-one linear regression results are provided in Table 6, which includes the same statistical descriptors presented earlier. Note that here we evaluated the same observations presented in the ρ_t validation (Section 3.2.2). Overall, SD-MSI R_{rs} difference for the visible bands was 16%–95%. R_{rs}(705) exhibited highest discrepancies of ~95% while green band (R_{rs}(565)) consistency was within ~16% followed by blue band (R_{rs}(490)) with ~32% MPD. The coastal blue (R_{rs}(443)) and red (R_{rs}(665)) bands showed ~60% differences with similar error bars.

The consistency in SD-MSI R_{rs} products following the calibration update was also assessed. For that, SD R_{rs} products were retrieved from ACOLITE after applying calibration parameters (developed in section 3.2.1) to the SD ρ_t data. Figure 5B illustrates the SD-MSI R_{rs} differences after applying calibration, and the linear regression statistics are presented in Table 7. Figures 5A,B and Tables 6 and 7 present the differences in SD-MSI R_{rs} before and after applying calibration to the SD ρ_t observations, respectively. Figures 5A,B show the reduction in MPDs for most of the spectral bands following cross-calibration with MSI. More specifically, for the coastal blue band (R_{rs}(443)), MPD was reduced to ~40% from

TABLE 7 The SuperDove (SD) - Multispectral Imager (MSI) remote sensing reflectance (R_{rs}) product inter-consistency metrics generated from the near-simultaneous validation dataset (after calibration) using ACOLITE atmospheric correction (AC) processor. Note that the R_{rs} products are compared over the same matchup sites used for top-of-atmosphere (TOA) reflectance (ρ_t) validation. The $\bar{R}_{rs,MSI}$ and $\sigma_{R_{rs,MSI}}$ represents the average MSI R_{rs} for the matchups, and standard deviation, respectively.

Band [nm]	N	$\bar{R}_{rs,MSI}$	$\sigma_{R_{rs,MSI}}$	Slope	Intercept	R^2	RMSD	Bias	MD	MPD [%]	MAD [%]
443	5,994	0.009	0.004	0.8453	0.00560	0.889	4.6E-03	4.1E-03	4.8E-03	40	17
490	16,266	0.011	0.005	0.8653	0.00458	0.986	3.3E-03	3.2E-03	3.3E-03	35	15
565	14,889	0.012	0.003	0.8066	0.00373	0.927	2.0E-03	1.4E-03	0.9E-03	8	13
665	16,803	0.005	0.001	0.8502	0.00429	0.602	4.1E-03	3.6E-03	2.6E-03	61	47
705	16,654	0.004	0.001	1.1728	0.00176	0.776	2.7E-03	2.4E-03	2.3E-03	72	45

~60%, RMSD decreased to 4.6E-03 from 6.3E-03, and bias and MD were reduced by ~2.0E-03. The red-edge band (R_{rs}(705)) also showed modest reduction in MPD, which decreased to ~72% from ~95%. RMSD, bias and MD were also reduced for this band (refer to Tables 6 and 7). MPDs of R_{rs}(565) were reduced by a factor of 2, from 16% to 8%, indicating better consistency in SD-MSI R_{rs} following calibration. R_{rs}(490) and R_{rs}(665) exhibited slight increases in MPDs, which may be attributed to the inherent uncertainty in the ACOLITE AC processor (Pahlevan et al., 2021; Vanhellemont, 2023; 2019b; Vanhellemont and Ruddick, 2018). Overall, following calibration applied to ρ_t, SD-MSI R_{rs} difference was 8%–72%.

3.3.2 Qualitative R_{rs} comparison

To visualize the differences in the ACOLITE-derived SD-MSI R_{rs} products, we have processed three SD-MSI near-simultaneous (within 6–10 min) image pairs collected over the Chesapeake Bay, Boodalan Nature Reserve in Western Australia, and Atlantic Ocean (U.S. East Coast). These images were selected over these inland and coastal bodies of water to assess the R_{rs} products retrieved from SD and improvement after applying cross-calibration.

Figure 6 shows the R_{rs} maps over the Chesapeake Bay (Honga River) on 19 Feb 2024, with the upper panels illustrating the MSI products, and the middle and lower panel depicting the SD and calibrated SD products, respectively. From the MSI and "as-is" SD maps, it is evident that the SD R_{rs} product's magnitude is higher than MSI R_{rs} in all the presented bands. Note that the ΔVZA for this image pair is ~ 2° and ΔRAA is approximately 10°, which could partially contribute to the differences in SD-MSI R_{rs}. The calibration applied to the SD has reduced the R_{rs} magnitude in all bands (refer to bottom panel), indicating better agreement with MSI. The most apparent decrease in R_{rs} can be noticed in the blue band (443 and 490 nm), while slight decreases were observed in the red-edge band (705 nm). Note the pronounced striping artifacts in the western portion of the SD R_{rs} (705), which were reduced after calibration. The calibrated SD R_{rs} for the green and red (565 and 665 nm) bands exhibited lower visual difference with MSI R_{rs} compared to un-calibrated R_{rs} of SD. Overall, these findings align with the analysis presented in Section 3.3.1.

To further demonstrate the R_{rs} retrieval differences, SD-MSI image pairs over the Boodalan Nature Reserve in Western Australia collected on 15 Feb 2024 (Figure 7), and over the Atlantic Ocean (U.S. East Coast–Pamlico Sound, North Carolina) on 26 Feb 2024 (Figure 8), were processed. Figures 7, 8 illustrate the MSI, "as-is" SD, and calibrated SD R_{rs} maps. A closer examination of the maps reveals that "as-is" SD products are brighter than MSI for all the bands, while applying calibration to SD reduced the magnitude of SD R_{rs} for all the bands, except 665 nm. Most evident is a decrease in R_{rs} which can be noticed in the 443 and 705 nm bands, whereas a slight reduction of SD R_{rs} magnitude was observed in the 490 and 565 nm bands. To completement the visual interpretation, R_{rs} spectra were produced by averaging R_{rs} within 100 × 100 MSI pixels (and corresponding SD pixels) over the red box shown in MSI 443 nm (refer to MSI 443 nm of Figures 7, 8). Figures 9A,B show the magnitude of SD R_{rs}(443) and R_{rs}(705) were reduced the most compared to other bands following calibration update, which agrees with the analysis presented in Section 3.3.1. The magnitudes of SD R_{rs}(490) and R_{rs}(565) were decreased, while slight increase was observed for the red band (R_{rs}(665)).

Overall, the qualitative visual comparisons presented in Section 3.3.2 were largely consistent with the quantitative assessment in Section 3.3.1, particularly for bands 443, 565, and 705 nm, which showed notable improvements after calibration. However, minor discrepancies were observed in a few scenes, likely due to inherent uncertainties in the ACOLITE atmospheric correction process, such as view angle differences or sensor striping artifacts (refer to Section 4 for further discussion).

3.4 Water quality products

This section investigates the effect of calibration on the water quality (WQ) maps—specifically Chl*a* and Z_{sd} —generated using SD data. WQ maps generated from the original SD data are referred to as ***'SD'***, while those generated from the calibrated SD data are referred to as ***'SD-cal'*** in the following sections. The assessment includes a visual comparison of these products with corresponding WQ maps derived from near-concurrent MSI measurements, highlighting the potential use of the calibrated SD products—characterized by high frequency and near-daily temporal resolution—for supporting aquatic science and monitoring activities. Additionally, we compare the WQ time series derived from SD and SD-cal data to those from MSI, illustrating the utility of the SD constellation for tracking aquatic responses to localized events such as wildfires.

3.4.1 Visual assessments

In this section, we present a qualitative comparison of SD and SD-cal derived WQ maps to the near-simultaneous MSI-derived

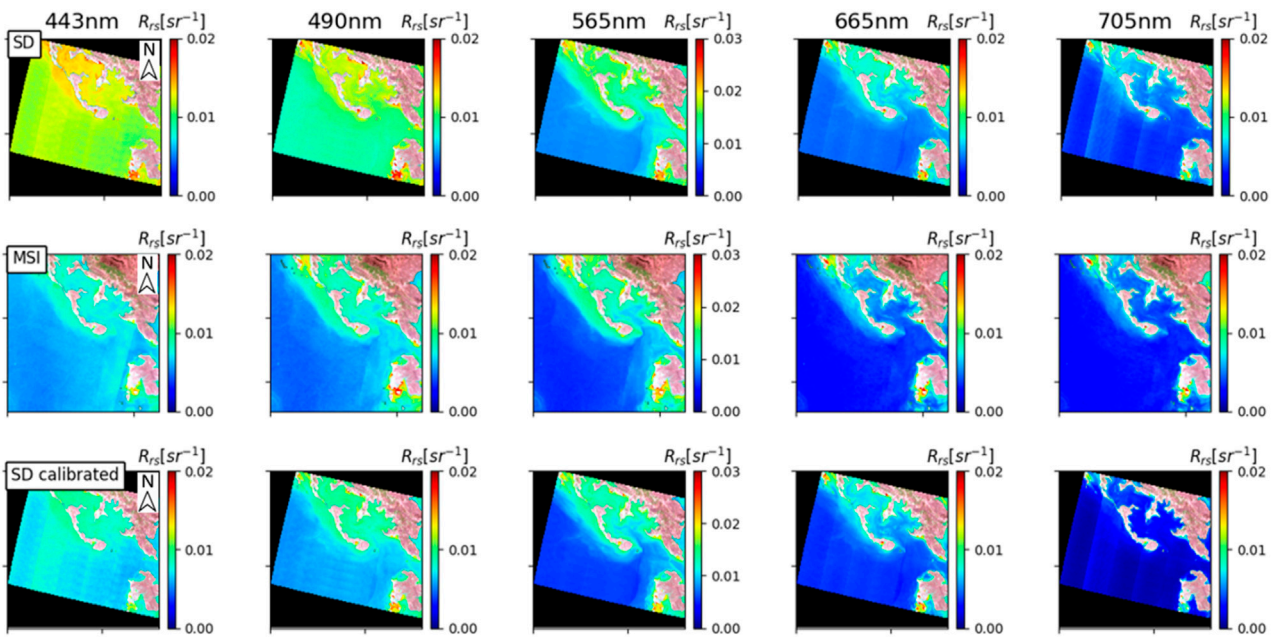

FIGURE 6
SuperDove (SD) and Multispectral Imager (MSI) remote sensing reflectance (R_{rs}) maps (over Honga River in Chesapeake Bay watershed imaged on 19 Feb 2024) for the five visible bands. The SD and MSI R_{rs} products exhibited varying degrees of differences for all the bands. Applying calibration to the SD observation reduced the R_{rs} differences with MSI products, which is apparent for all the bands.

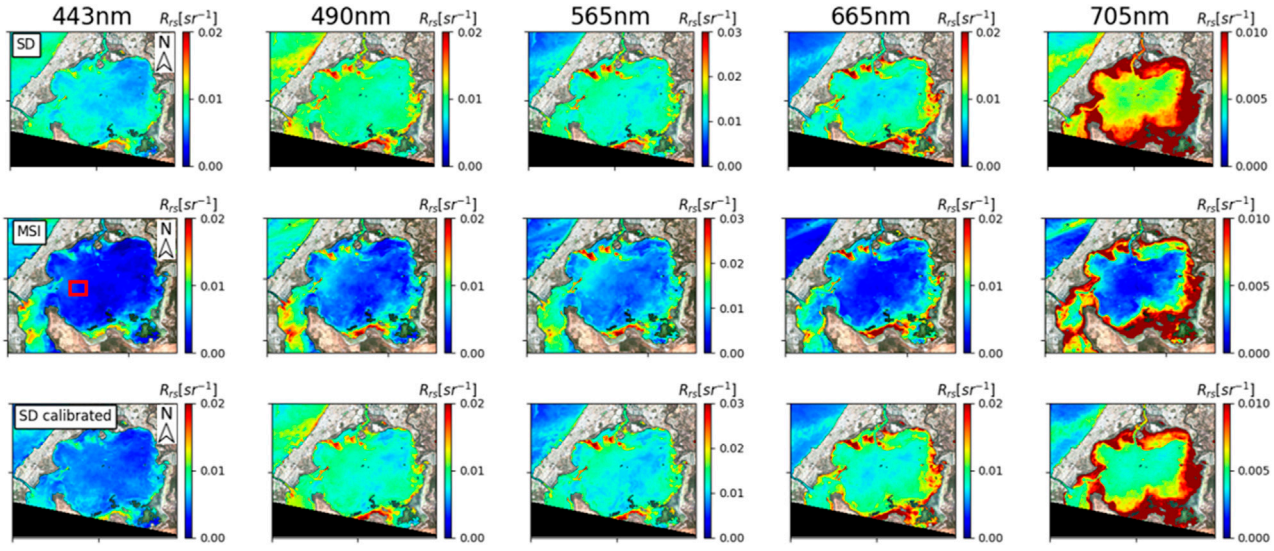

FIGURE 7
ACOLITE-derived SuperDove (SD) and Multispectral Imager (MSI) remote sensing reflectance (R_{rs}) maps (over Boodalan Nature Reserve in Western Australia imaged on 15 Feb 2024) for the five visible bands. The MSI and SD R_{rs} products exhibiting varying degrees of differences for all the bands. Applying calibration to the SD observation reduced the differences, which is apparent for 443 and 705 nm bands. Spectra from the red box in the top left panel are plotted in Figure 9A.

WQ maps to get a general sense of the SD model's ability to generate quality downstream products for WQ monitoring. The WQ maps for Boodalan Nature Reserve (Western Australia), Lake Almanor (California, United States), and Chesapeake Bay (eastern United States) are shown in Figures 10–12, respectively.

The Chl*a* for Boodalan Nature Reserve (top row of Figure 10) shows consistent spatial trends across all three maps, with heightened Chl*a* in nearshore regions but lower Chl*a* at the center of the waterbody. The uncalibrated SD maps show consistently higher values than the MSI maps in both nearshore

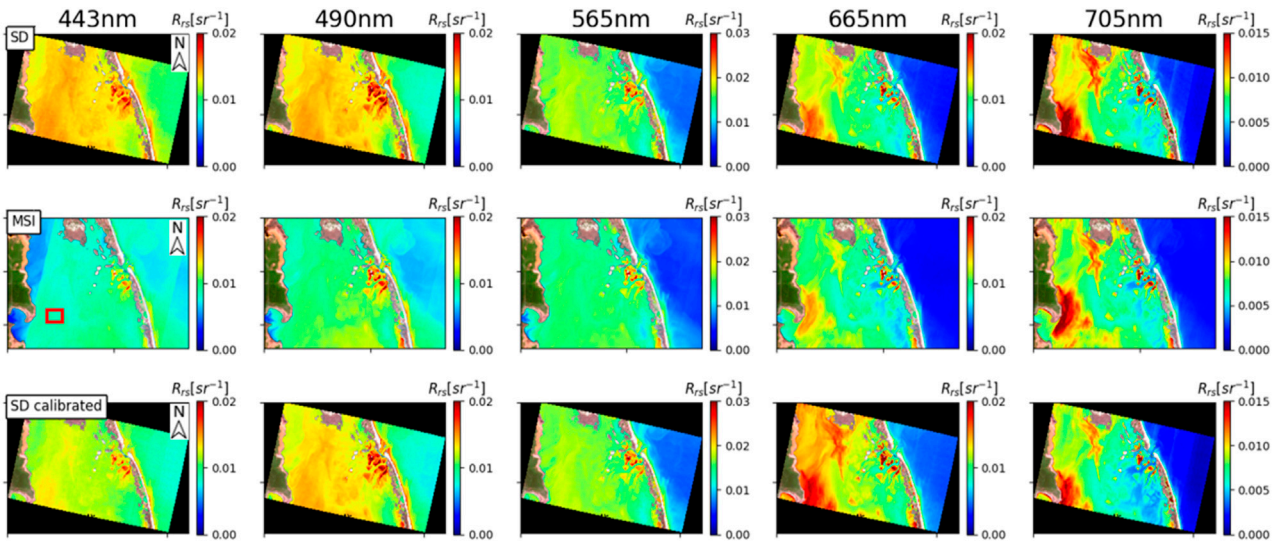

FIGURE 8
ACOLITE-derived SuperDove (SD) and Multispectral Imager (MSI) remote sensing reflectance (R_{rs}) maps (over the Atlantic Ocean, U.S. East Coast–Pamlico Sound, North Carolina imaged on 26 Feb 2024) for the five visible bands. Applying calibration to the SD observation reduced the R_{rs} differences, which is apparent for 443 and 705 nm band. Spectra from red box in the middle left panels are plotted in Figure 9B.

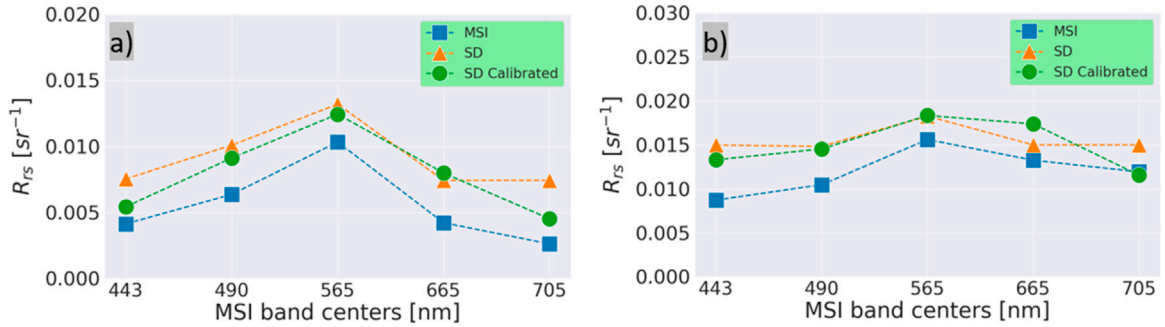

FIGURE 9
Mean SuperDove (SD) and Multispectral Imager (MSI) remote sensing reflectance (R_{rs}) spectra for the visible bands over the red boxes in: **(a)** Figure 7, **(b)** Figure 8. Reduction of SD-MSI R_{rs} difference after cross-calibration is noticeable for the 443 and 705 nm bands.

and central areas. Further, there are also differences in the spatial trends in the nearshore regions (especially in the regions highlighted by the red boxes). Post-calibration, these spatial differences were substantially diminished, even the central Chl*a* values for the calibrated map are moderately suppressed and more in agreement with the MSI maps. However, the Z_{sd} maps over Boodalan Natural Reserve also reveal regions where calibration does not fully resolve discrepancies, particularly over the lagoon, where Z_{sd} differences exceeding ±1 m persist. Such overestimations could be problematic for end users seeking precise water clarity information. While there was agreement on low Z_{sd} values nearshore and higher Z_{sd} in central regions, the SD-estimated Z_{sd} are consistently lower than the corresponding MSI-estimated Z_{sd}. Nevertheless, there is a clear correlation between the Chl*a* and Z_{sd} maps, and areas with high Chl*a* correspond to low Z_{sd} and *vice versa* (note that the color-bar for Z_{sd} is the inverse of the one used for Chl*a*). Further, the scale for the Z_{sd} maps is narrow, so we should not over-interpret the color differences in these maps. Similarly, in Figure 11, with the maps over Lake Almanor, California, we observe heightened Chl*a* and reduced Z_{sd} in the main body of the lake for the SD uncalibrated products; the differences were substantially reduced/suppressed after the calibration. Figure 12 over the Chesapeake Bay shows the effect of calibration on WQ maps derived from noisy images, while both SD-cal maps continue to show some noise and calibration effects these are less pronounced than in the uncalibrated WQ maps.

Post-calibration, the spatial trends for the various WQI from both products generally agree more than before calibration. While this appears to be true based on our qualitative analysis, this may not always be the case. An example where the calibration does not seem to suppress the differences between the MSI and SD-generated WQ products is shown in Figure 12 for maps of Chesapeake Bay. Again, while there is general agreement regarding higher Chl*a* and lower Z_{sd} values near shore and higher Z_{sd} and lower Chl*a* values over the

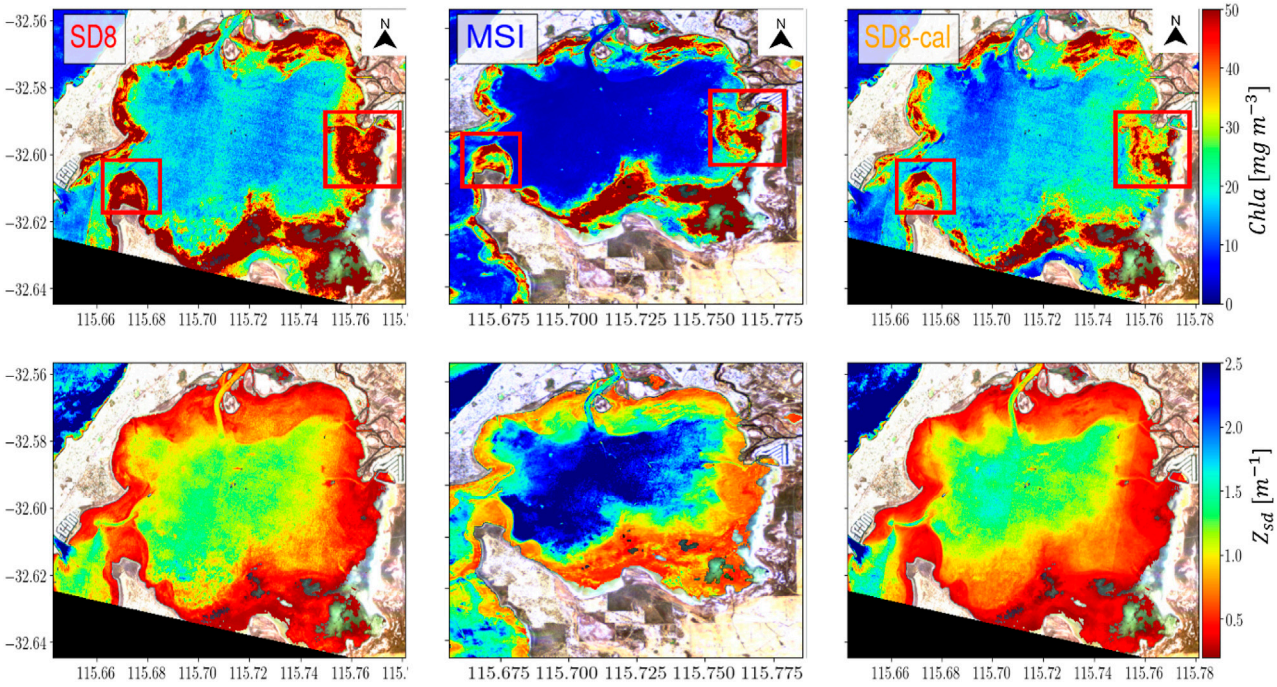

FIGURE 10
Effect of calibration on mixture density network (MDN) generated Chl*a* (top row) and Secchi-disk-depth (Z_{sd}) (bottom) maps over the Boodalan Nature Reserve in Western Australia, the figure shows uncalibrated SuperDove (SD: left col), Multispectral Imager (MSI: middle column), and calibrated SD (SD-cal). Both MSI and SD images were acquired on 15 Feb 2024, and processed to R_{rs} *via* ACOLITE. The red boxes in the top column identify specific location where the SD-cal water quality (WQ) maps shows improved agreement with the MSI maps.

open bay, the MSI Chl*a* maps show higher values of Chl*a* than the calibrated SD maps. The Z_{sd} maps, on the other hand, show more agreement. A cursory analysis suggested that the uncalibrated or SD Chl*a* maps are more in line with the corresponding MSI maps. While noting these differences, another consideration is that the SD/MSI maps for this location appear quite noisy and are affected by other distortions observed in satellite data, such as striping, *etc.* The noise and distortions, in this case, make it difficult to perceive the true spatial distribution of the various WQIs. While calibration generally improves the agreement between MSI and SD derived WQ maps, substantial discrepancies remain in some cases, such as Boodalan Natural Reserve and Chesapeake Bay, where substantial discrepancies remain even after calibration. These should not be overlooked, especially for applications requiring high-accuracy water clarity estimates. These discrepancies could arise from multiple sources including the instability and inconsistencies across the multiple SD sensors (refer to Appendix D, Supplementary Figure SD1), AC processor, and model limitation (refer to Section 4 for discussion and future directions). The MSI WQ maps, while popular and often referenced for comparison, may be affected by uncertainties arising from similar sources, including AC, calibration, and algorithmic limitations.

3.4.2 Time-series analysis

To further demonstrate the utility of SD observations and MDN derived WQ parameters, we processed SD imagery that captured the impact of the Dixie Fire near Lake Almanor in California (https://www.fire.ca.gov/incidents/2021/7/13/dixie-fire). This wildfire event (started on 13 July 2021, and was fully contained on 25 Oct 2021) is known as the single largest wildfire in California history, which burned along the western shore of Lake Almanor. The Dixie Fire was immediately followed by eight inches of rainfall in just a few days in late Oct, which appeared to trigger an algal bloom in the lake (https://www.plumasnews.com/drought-and-dixie-fire-impacts-water-quality-at-lake-almanor/). The WQ product retrieval models, presented in Section 2.5 and inSupplementary Appendix C, were applied to SD observations (corrected with ACOLITE) to map Chl*a* and Z_{sd} over Lake Almanor. Figure 11 shows one Chl*a* and Z_{sd} product map of SD and MSI images collected on 30 Nov 2021.

Figure 13 showcases the potential of SD observations to monitor water quality in Lake Almanor in the form of a time series. This time-series analysis serves to illustrate the feasibility of using cross-calibrated SD observations for tracking short-term water quality dynamics. We processed available SD and MSI observations over the lake from September 15 to 20 Dec 2021, and plotted average Chl*a* and Z_{sd} within black box (limit = 40.249,147, −121.172,521, 40.255,412, −121.162,233) in Figure 11. The selected area consistently exhibited valid retrievals across both SD and MSI observations throughout the study period. This area lies within the central portion of Lake Almanor, avoiding edge effects, land contamination, and extreme glint artifacts, which can bias water quality estimates. It also encompasses a relatively homogenous water body that reflects broader lake conditions, making it suitable for temporal trend analysis and comparison between sensors. The number of observations is higher (2X) for SD than MSI, with 30 SD collects and 14 MSI images, showcasing the advantage of higher

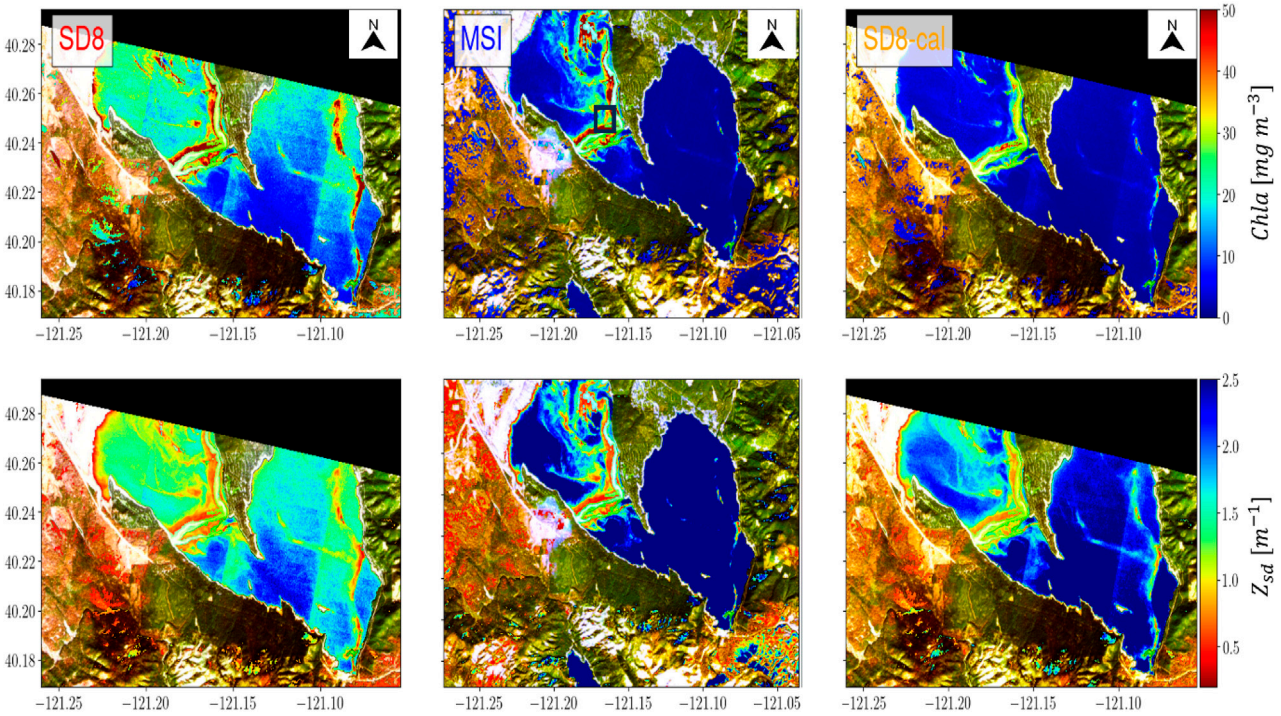

FIGURE 11
Effect of calibration on mixture density network (MDN) generated Chl*a* (top row) and Secchi-disk-depth (Z_{sd}) (bottom) maps over the Lake Almanor, the figure shows uncalibrated SuperDove (SD: left col), MSI (middle column), and calibrated SD (SD-cal). Both MSI and SD images were acquired on 30 Nov 2021, and processed to R_{rs} *via* ACOLITE. Across the whole spatial extent for both products the calibrated water quality (WQ) maps show improved agreement with the MSI WQ maps.

temporal resolution of SD. During the wildfire event (before 10–20), most of the Z_{sd} retrievals from SD and a few from MSI were on the order of ~2m, suggesting transparent water for this period. Following the heavy rain (from 10–20 to 10–27), the Z_{sd} was ~1 m (refer to 10–28 and 10–29), most likely due to the increased turbidity in the lake. Afterwards, Z_{sd} recovered (refer to 11–20 and 11–21) to ~2m, indicating improved water transparency. Pre-fire (before 10–20) Chl*a* concentration was found <20 $mg\,m^{-3}$, which increased after the rain event and algae bloom (after 10–27). The applied calibration to SD observations did not substantially change the Z_{sd} magnitude. However, Chl*a* concentrations were reduced for almost all the observations and followed the expected trends. Overall, the SD products captured the expected trend; however, the bias relative to the MSI product and some deviations from expected patterns may be attributed to uncertainties in ACOLITE and MDNs when producing Chl*a* and Z_{sd} from both MSI and SD (refer to Section 4 for discussion and future directions). While ACOLITE remains a widely used processor for aquatic remote sensing, its limitations, particularly in optically complex waters are well known. Alternative AC methods such as SeaDAS may offer better performance in specific environments. Future work could evaluate whether sensor-specific calibration of R_{rs}, independent of ρ_t, provides further improvements in water-quality product accuracy.

4 Discussions and future directions

We have presented the SNR assessment for the SD sensors to evaluate the noise performance (refer to Figure 2), including MSI SNRs reported in the literature. SD SNRs was slightly less than MSI for most of the bands (490, 565, 665 and 705 nm), whereas SD SNR for 443 nm is ~0.5× of MSI SNR. Lower SNRs in the SD might be partly due to their finer spatial resolution compared to MSI. In this work, we assumed the sensor sensitivity or SNR of different SD instruments were similar, which may need further investigation. To characterize the noise of different SD instrument-generated images, SNRs ideally should be evaluated sensor-by-sensor. Moreover, we examined the SNRs over clear water in Crater Lake, Oregon due to the lack of open ocean observations. Ideally, SNRs should be evaluated over different aquatic and atmospheric conditions, as precision in water quality products (e.g., Chl*a*, Z_{sd}, etc.) depends on the noise performance of the observations (Hu et al., 2001, 2012).

We attempted to cross-calibrate the SD constellation with near-simultaneous MSI observations over a broad range of aquatic ecosystems, with the aim of developing calibration coefficients for SD images. The cross-calibration and validation of the SD constellation showed that our calibration parameters reduced the differences in SD and MSI ρ_t observations on the validation dataset (refer to Figure 4). The initial assessment revealed that "as-is" SD observations were significantly different in some bands (refer to Figures 3, 4A) which reduced following the calibration update, confirming the validity of the calibration parameters (refer to Tables 4 and 5). However, due to the limited number of ideal matchups from each individual SD sensor, it was not possible to carry out sensor by sensor analysis. Additionally, for the same reason, it was also not feasible to analyze and perform calibration and validation activities by optical water types (OWTs). Future

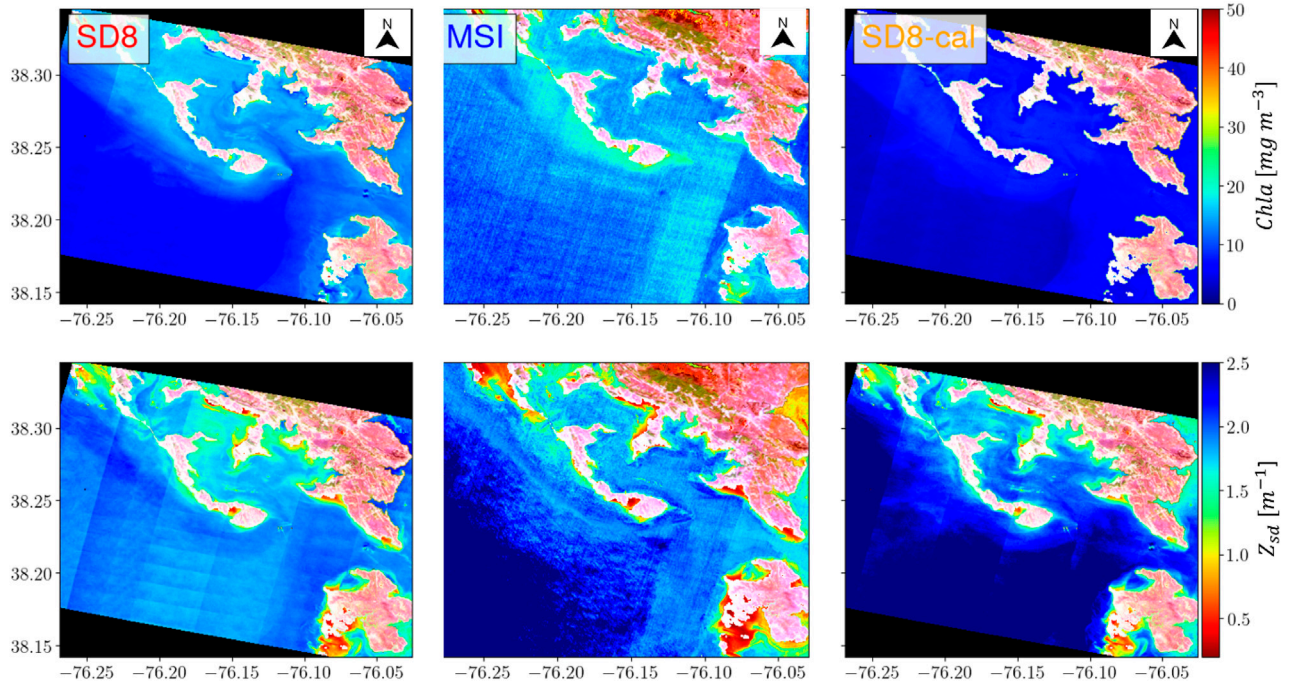

FIGURE 12
Effect of calibration on mixture density network (MDN) generated Chl*a* (top row) and Sechhi-disk-depth (Z_{sd}) (bottom) maps over the Chesapeake Bay, the figure shows uncalibrated SuperDove (SD: left col), MSI (middle column), and calibrated SD (SD-cal). Both MSI and SD images were acquired on Feb. 19th, 2024, and processed to R_{rs} *via* acolite. This is an illustration of the effect of the calibration on water quality (WQ) maps derived from a "noisy" image.

analysis could be improved by sensor-by-sensor and by different OWTs. This study did not include the 865 nm band due to inconsistent and noisy ρ_t data. If possible, future studies may also include 865 nm, along with the 531 and 610 nm bands to improve outcomes. Note that the developed cross-calibration parameters might need adjustments/improvements as radiometric stability of different SD sensors can vary (Lavender, 2024).

A fundamental limitation arises from the instability and inconsistencies across the multiple SD sensors. The PlanetScope constellation includes over 200 SD units, each exhibiting slight variations in radiometric behavior. Our analysis focused on a subset of 11 SD units, selected to be representative of the broader constellation in terms of geographic distribution and sensor behavior, while also keeping the analysis tractable. We observed substantial per-sensor variability in the relative differences between SD and MSI ρ_t, with median biases varying significantly across sensors (refer to Appendix D, Supplementary Figure SD1). These discrepancies suggest that sensor-to-sensor inconsistencies are a dominant contributor to the observed mismatch, beyond what improved AC methods alone can resolve. While sensor harmonization across the SuperDove constellation is a critical next step toward addressing this issue, it was beyond the scope of this study, which focused on assessing the feasibility and initial performance of SD imagery for aquatic applications. Future research may explore the implementation and evaluation of cross-sensor harmonization strategies to reduce inter-sensor discrepancies and enhance the consistency of water-quality retrievals from SD data.

We have also evaluated the ACOLITE-derived SD R_{rs} products against MSI R_{rs} products. We found large R_{rs} differences with MSI which were reduced after calibration of SD data (refer to Figure 5). However, for most of the bands, the residual differences in R_{rs} products were >40% (refer to Figure 5B) despite <3% ρ_t differences (Figure 4B) after applying calibration. This suggests that the ACOLITE AC processors most likely were not generating consistent R_{rs} products from SD observations, as ACOLITE-derived MSI R_{rs} products are typically consistent (Pahlevan et al., 2021). Note that the mean absolute relative difference of ACOLITE-derived R_{rs} and *in situ* observations over near-shore turbid water in a Belgian coastal zone (southern North Sea) was ~20% for the visible bands (Vanhellemont, 2023). We surmise that the existing ACOLITE processor has the potential to be validated and improved over a wide range of optical regimes and/or AC schemes could be developed for the SD sensors that provide consistent retrieval of R_{rs}.

The uncertainties in the cross-calibration and validation could arise from several different sources, including RSR function adjustment, spatial resolution mismatch, cloud, cloud shadow, and haze related noises, sun/sky glint, land-water adjacency effect, and high aerosol loading. This study assumed the RSR function related SD-MSI difference to be minimal since SD TOA reflectance products are calibrated to MSI TOA reflectance before disseminating SD data to the user (P. Team, 2022) and that the RSR of SD and MSI are nearly identical (Tu et al., 2022). However, future studies should investigate the RSR related differences in the ρ_t and downstream products over wide range of aquatic ecosystems. Despite using averages over a relatively large area (7 × 7 MSI pixels), SD-MSI spatial resolution mismatches may introduce some uncertainties. To discard the cloud, cloud shadow, and haze from SD and MSI images, we have exploited UDM2 from

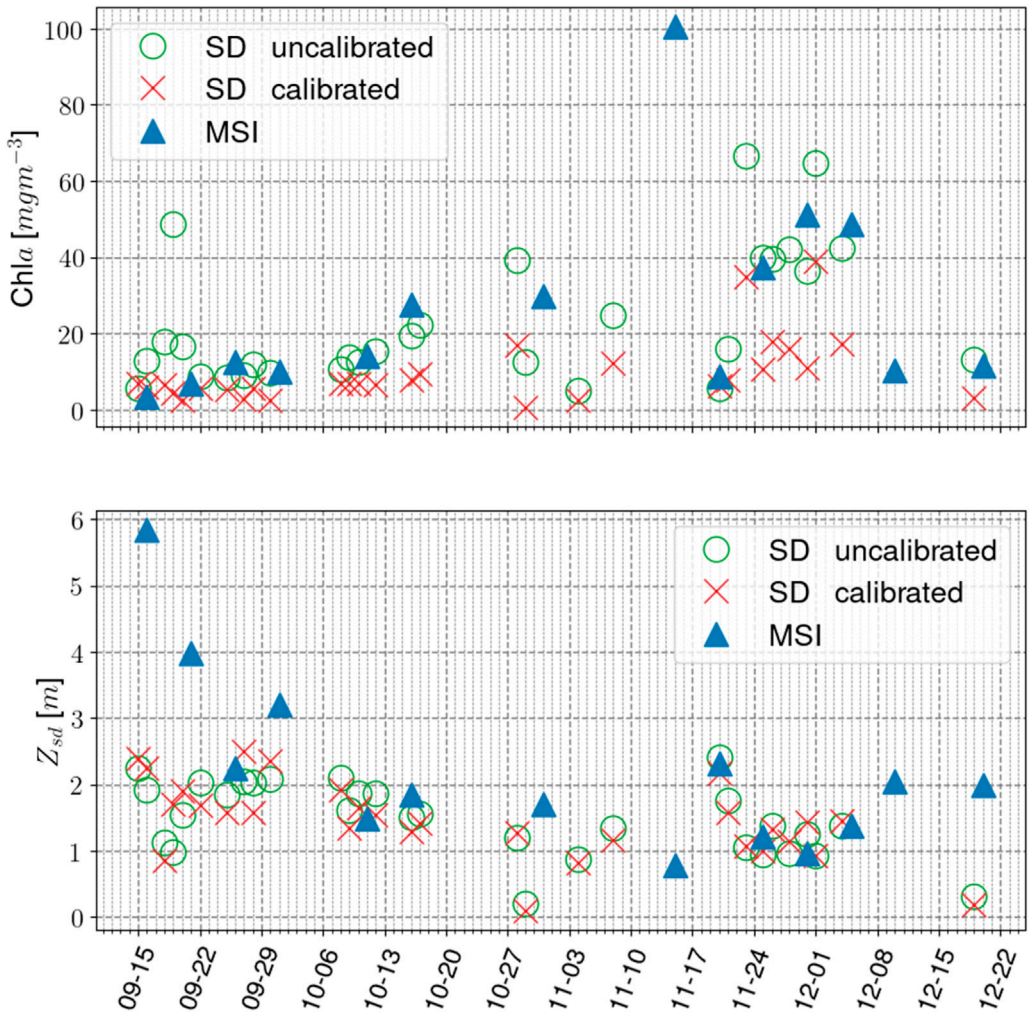

FIGURE 13
SuperDove (SD) and Multispectral Imager (MSI) Chl*a* (top row) and Sechhi-disk-depth (Z_{sd}) (bottom row) time-series for Lake Almanor averaged over the region identified by the black box in Figure 11, for the period September 15 to 20 Dec 2021, that includes a Dixie Fire event (before October 20) and heavy rainfall (October 20–27) events. There were 30 SD images available, while 14 MSI images were found over this period. The time series from the two sensors generally agree highlighting the ability to leverage the high temporal resolution of the SD data for monitoring the effect of these episodic events on water bodies.

SD, ACOLITE L2 flags for SD and MSI. Even though these masks remove impacted pixels to a certain extent, some of the matchup sites might be affected by thin clouds, cloud shadows, haze, *etc.* However, the associated impact on the overall uncertainty is believed to be minimal, as most of the data points were free from cloud, cloud shadow, and haze. The land-water adjacency effects (Bulgarelli et al., 2014) and sun/sky glint (Gilerson et al., 2018) could introduce some uncertainties despite using L2 flags. High differences in the R_{rs} products (~40%) could be partially due to the uncertainty in the aerosol removal (Gordon et al., 1997). However, in general, ACOLITE retrieval uncertainty is believed to be the primary reason for the >40% differences (refer to Figure 5B).

To demonstrate the potential of SD observations for aquatic science and applications, we applied ML based MDN models to retrieve Chl*a* and Z_{sd}, and presented a visual comparison of MSI *versus* SD-derived Chl*a* and Z_{sd} product. The results indicated generally improved agreement in the MSI and SD Chl*a* and Z_{sd} maps following calibration in the presented image pairs. However, this process is not able to completely eliminate all disagreements between WQ maps from the two sources. These differences indicate that the calibration (based on a correction of the systematic differences between the MSI and SD) cannot, in the presence of noise and uncertainties in the atmospheric correction, correct for all discrepancies between the MSI and SD-derived WQ maps. Furthermore, while the legacy MSI data have been better studied and characterized, they are not ideal/noise-free. While MSI is a reference point for comparison, it is also subject to uncertainties. The uncertainties in the WQ product maps are further affected by the accuracies of the cloud-masking and AC processing of the two different datasets, and improved AC processing using advanced methods could help further minimize the local variations between the MSI and SD derived WQI maps. Overall, there is an agreement between the MSI and SD maps (especially post calibration), indicating that these products can be used in concert with other sensors such as L8/L9, Sentinel-2, for WQ monitoring. While the selected examples in Figures 10–12 focus on clear and moderately turbid waters, they were

chosen for their high data quality and availability of near-concurrent SD and MSI observations. Extending this analysis to include highly turbid or optically complex systems may be explored in the future work as more diverse matchups become available. Further, the time-series analysis of the SD and MSI observations was also processed around the Dixie Fire event in Lake Almanor, California. The Chl*a* and Z_{sd} values from SD showed similar trends. However, the biases in SD estimates relative to the MSI-derived products (refer to Figure 13) were not largely affected by the calibration. As such, the differences are not due to consistent differences between the SD and MSI sensors but are rather affected by random effects like sensor noise, imperfect AC processing, and or cloud masking, which need to be better addressed to further minimize these differences (Pahlevan et al., 2024; Zolfaghari et al., 2023). However, the time-series trend aligned with patterns typically observed before and after the heavy rainfall over the lake, suggesting that SD observations may support the monitoring episodic event-related WQ variability. While this example demonstrates the applicability of SD imagery for aquatic context, further quantitative assessment is necessary to evaluate the use of WQ products from SD observations. Specifically, to comprehend the full capability of SD observations and retrieval algorithms, WQ products, such as Chl*a*, Z_{sd}, TSS, a_{cdom}, *etc.*, can be generated over diverse aquatic conditions and validated against *in situ* measurements. While this study primarily validated SD-derived products relative to MSI, future work may incorporate matchup datasets with *in situ* measurements of Chl*a* and Z_{sd}. These efforts may enable assessment of absolute accuracy and strengthen the utility of SD products within operational water-quality monitoring frameworks.

5 Summary and conclusion

This study described the radiometric cross-calibration and validation of SD ρ_t against well-calibrated MSI ρ_t observations over aquatic ecosystems from across the globe. We exploited near-simultaneous SD-MSI ($\Delta T < 10$ min) observations to obtain calibration parameters (i.e., gains and offsets) through regression analysis. Before applying the calibration, we found 0.7%–13% differences in SD-MSI ρ_t, with the red (665 nm) and red-edge (705 nm) bands exhibiting the highest differences of ~8% and ~13%, respectively. After applying the calibration to SD ρ_t, the SD-MSI discrepancies were reduced from −2.2% to −0.7%. Specifically, SD-MSI differences in ρ_t (665) and ρ_t (705) were reduced from ~8% to −2.2%, and from ~13% to −0.1%, respectively. The coastal-blue band (ρ_t (443)) discrepancy decreased from 1.4% to −0.07%. However, only slight changes (<0.4%) were observed for the 490 and 565 nm bands, with MDP shifting from 0.7% to −1.1% for ρ_t (490) and −1.6% to −1.8% for ρ_t (565). Overall, the calibration update reduced the SD-MSI ρ_t differences to within −2.2%, with the highest residual discrepancy in ρ_t (705), and the best agreement in ρ_t (443) at −0.07%. The ACOLITE-derived SD-MSI R_{rs} differences ranged from 16% to 95%, which were reduced to 8%–72% after applying the calibration. Among the bands, R_{rs} (565) exhibited the lowest difference (~8%), while the 705 nm band showed the highest (~72%). These large differences in the R_{rs} products are believed to be partly attributed to uncertainties in the ACOLITE-derived SD R_{rs} retrievals. This study also presented SNR estimates to quantify the noise characteristics of SD observations. While this study assumes a consistent SNR model across SD units, variability in sensor radiometry has been observed across the constellation. Future work may aim to characterize sensor-specific noise using a broader sample of SD units to better constrain calibration performance and quantify instrument-to-instrument variability. We found the highest SNR of 248 in the 443 nm band, with the NIR band exhibiting the lowest SNR (~8), and the other visible bands ranging from 26 to 98. To demonstrate the utility of SD observations for water quality applications, this study presented visual assessments over select locations and a time-series analysis focused on the Dixie Fire and associated algal bloom (from September to December 2021) in Lake Almanor, California. The results showed that SD-derived Z_{sd} products improved after calibration, with some exceptions, and the time series successfully captured expected trends. While the calibration coefficients improve the radiometric agreement between SD and MSI in terms of ACOLITE-corrected TOA reflectance and R_{rs}, this does not necessarily result in proportional improvements in the agreement of downstream water quality products. Further quantitative evaluations using *in situ* R_{rs} and corresponding product matchups can assess this. Since a major source of residual discrepancy in R_{rs} and downstream products is the atmospheric correction process, particularly in optically complex waters, future efforts may focus on improving AC algorithms for these environments to fully leverage the radiometric calibration. Additionally, this study did not explicitly stratify calibration by OWTs, which could affect performance in underrepresented water classes. Most matchups were concentrated in mesotrophic and estuarine systems, and future calibration schemes can incorporate OWT-specific stratification to enhance global applicability. Nonetheless, this study demonstrates the feasibility of using cross-calibrated SD data to complement Sentinel-2 observations and enhance temporal resolution for aquatic monitoring in data-sparse time windows.

Data availability statement

The data analyzed in this study is subject to the following licenses/restrictions: The commercial Planet SuperDove satellite is subject to data availability and access regulations. Requests to access these datasets should be directed to https://csdap.earthdata.nasa.gov/.

Author contributions

SK: Investigation, Software, Methodology, Formal Analysis, Data curation, Visualization, Writing – original draft. AS: Writing – review and editing, Software. BB: Writing – review and editing. AA: Writing – review and editing, Project administration. RO'S: Writing – review and editing. VS: Writing – review and editing.

Funding

The author(s) declare that financial support was received for the research and/or publication of this article. This project was funded

by NASA's Commercial Smallsat Data Scientific Analysis (CSDA) program, grant # 80NSSC24K0049.

Acknowledgments

We acknowledge Nima Pahlevan (NASA Headquarters) and Keith Bouma-Gregson (USGS) for their contributions to the development of this study. Any use of trade, product, or firm names is for descriptive purposes only and does not imply endorsement by the U.S. Government.

Conflict of interest

Authors SK, AS, AA, RO'S were employed by Science Systems and Applications, Inc.

The remaining authors declare that the research was conducted in the absence of any commercial or financial relationships that could be construed as a potential conflict of interest.

Generative AI statement

The author(s) declare that no Generative AI was used in the creation of this manuscript.

Publisher's note

Supplementary material

The Supplementary Material for this article can be found online at: https://www.frontiersin.org/articles/10.3389/frsen.2025.1624783/full#supplementary-material

References

Balasubramanian, S. V., O'Shea, R. E., Saranathan, A. M., Begeman, C. C., Gurlin, D., Binding, C., et al. (2025). Mixture density networks for re-constructing historical ocean-color products over inland and coastal waters: demonstration and validation. *Front. Remote Sens.* 6, 1488565. doi:10.3389/frsen.2025.1488565

Balasubramanian, S. V., Pahlevan, N., Smith, B., Binding, C., Schalles, J., Loisel, H., et al. (2020). Robust algorithm for estimating total suspended solids (TSS) in inland and nearshore coastal waters. *Remote Sens. Environ.* 246, 111768. doi:10.1016/j.rse.2020.111768

Barnes, B. B., Hu, C., Bailey, S. W., Pahlevan, N., and Franz, B. A. (2021). Cross-calibration of MODIS and VIIRS long near infrared bands for ocean color science and applications. *Remote Sens. Environ.* 260, 112439. doi:10.1016/j.rse.2021.112439

Bishop, C. M. (1994). Mixture density networks. Birmingham, United Kingdom Aston University.

Bulgarelli, B., Kiselev, V., and Zibordi, G. (2014). Simulation and analysis of adjacency effects in coastal waters: a case study. *Appl. Opt.* 53, 1523–1545. doi:10.1364/ao.53.001523

Caballero, I., and Stumpf, R. P. (2019). Retrieval of nearshore bathymetry from Sentinel-2A and 2B satellites in south Florida coastal waters. *Estuar. Coast Shelf Sci.* 226, 106277. doi:10.1016/j.ecss.2019.106277

Cao, Z., Ma, R., Liu, M., Duan, H., Xiao, Q., Xue, K., et al. (2022). Harmonized chlorophyll-a retrievals in inland lakes from Landsat-8/9 and Sentinel 2A/B virtual constellation through machine learning. *IEEE Trans. Geoscience Remote Sens.* 60, 1–16. doi:10.1109/tgrs.2022.3207345

Collison, A., Jumpasut, A., and Bourne, H. (2021). On-Orbit Radiometric Calibration of the planet satellite fleet. Available online at: https://assets.planet.com/docs/radiometric_calibration_white_paper.pdf (Accessed July 24, 2025).

De Keukelaere, L., Sterckx, S., Adriaensen, S., Knaeps, E., Reusen, I., Giardino, C., et al. (2018). Atmospheric correction of Landsat-8/OLI and Sentinel-2/MSI data using iCOR algorithm: validation for coastal and inland waters. *Eur. J. Remote Sens.* 51, 525–542. doi:10.1080/22797254.2018.1457937

Fernandez-Saldivar, J., Pritchett, C., Ozawa, K., and Zuleta, I. (2020). Focus characterization of SuperDoves: On-ground and On-orbit first light.

Fickas, K. C., O'Shea, R. E., Pahlevan, N., Smith, B., Bartlett, S. L., and Wolny, J. L. (2023). Leveraging multimission satellite data for spatiotemporally coherent cyanoHAB monitoring. *Front. Remote Sens.* 4, 1157609. doi:10.3389/frsen.2023.1157609

Frazier, A. E., and Hemingway, B. L. (2021). A technical review of planet smallsat data: practical considerations for processing and using planetscope imagery. *Remote Sens. (Basel)* 13, 3930. doi:10.3390/rs13193930

Gilerson, A., Carrizo, C., Foster, R., and Harmel, T. (2018). Variability of the reflectance coefficient of skylight from the ocean surface and its implications to ocean color. *Opt. Express* 26, 9615–9633. doi:10.1364/oe.26.009615

Gordon, H. R. (1987). Calibration requirements and methodology for remote sensors viewing the ocean in the visible. *Remote Sens. Environ.* 22, 103–126. doi:10.1016/0034-4257(87)90029-0

Gordon, H. R., Du, T., and Zhang, T. (1997). Remote sensing of ocean color and aerosol properties: resolving the issue of aerosol absorption. *Appl. Opt.* 36, 8670–8684. doi:10.1364/ao.36.008670

Hu, C., Carder, K. L., and Muller-Karger, F. E. (2001). How precise are SeaWiFS ocean color estimates? Implications of digitization-noise errors. *Remote Sens. Environ.* 76, 239–249. doi:10.1016/s0034-4257(00)00206-6

Hu, C., Feng, L., Lee, Z., Davis, C. O., Mannino, A., McClain, C. R., et al. (2012). Dynamic range and sensitivity requirements of satellite ocean color sensors: learning from the past. *Appl. Opt.* 51, 6045–6062. doi:10.1364/ao.51.006045

IOCCG (2012). Mission requirements for future ocean-colour sensors. Dartmouth, NS: Reports of the International Ocean-Colour Coordinating Group.

Jumpasut, A., Collison, A., and Zuleta, I. (2020). On-orbit validation of interoperability between Planet SuperDoves and Sentinel-2.

Kabir, S., Leigh, L., and Helder, D. (2020). Vicarious methodologies to assess and improve the quality of the optical remote sensing images: a critical review. *Remote Sens. (Basel)* 12, 4029. doi:10.3390/rs12244029

Kabir, S., Pahlevan, N., O'Shea, R. E., and Barnes, B. B. (2023). Leveraging Landsat-8/-9 underfly observations to evaluate consistency in reflectance products over aquatic environments. *Remote Sens. Environ.* 296, 113755. doi:10.1016/j.rse.2023.113755

Kuhn, C., de Matos Valerio, A., Ward, N., Loken, L., Sawakuchi, H. O., Kampel, M., et al. (2019). Performance of Landsat-8 and Sentinel-2 surface reflectance products for river remote sensing retrievals of chlorophyll-a and turbidity. *Remote Sens. Environ.* 224, 104–118. doi:10.1016/J.RSE.2019.01.023

Lavender, S. (2024). European Space Agency (ESA). Technical Note on Quality Assessment for Planet SuperDove. Available online at: https://earth.esa.int/documents/d/earth-online/technical-note-on-quality-assessment-for-superdove-apr-2024 (Accessed July 24, 2025).

Lee, Z., Shang, S., Qi, L., Yan, J., and Lin, G. (2016). A semi-analytical scheme to estimate Secchi-disk depth from Landsat-8 measurements. *Remote Sens. Environ.* 177, 101–106. doi:10.1016/j.rse.2016.02.033

Lewis, M. D., Jarreau, B., Jolliff, J., Ladner, S., Lawson, T. A., McCarthy, S., et al. (2023). Assessing planet nanosatellite sensors for Ocean color usage. *Remote Sens. (Basel)* 15, 5359. doi:10.3390/rs15225359

Li, J., and Chen, B. (2020). Global revisit interval analysis of Landsat-8-9 and Sentinel-2A-2B data for terrestrial monitoring. *Sensors* 20, 6631. doi:10.3390/s20226631

Maciel, D. A., Pahlevan, N., Barbosa, C. C. F., Martins, V. S., Smith, B., O'Shea, R. E., et al. (2023). Towards global long-term water transparency products from the Landsat archive. *Remote Sens. Environ.* 299, 113889. doi:10.1016/j.rse.2023.113889

McCarthy, S., Lewis, M. D., Lawson, A., Martinolich, P., Jolliff, J. K., and Ladner, S. (2023). "Current Ocean color processing capabilities of planet's nanosatellite data within nrl's automated processing System," in OCEANS 2023-MTS/IEEE US Gulf Coast. Biloxi, MS: IEEE, 1–6.

Mobley, C. D. (1999). Estimation of the remote-sensing reflectance from above-surface measurements. *Appl. Opt.* 38 (36), 7442–7455. doi:10.1364/ao.38.007442

NASA Earth Science Division (2020). Commercial Smallsat Data Acquisition Program (CSDAP). Commercial smallsat data evaluation report. NASA Earthdata. Available online at: https://www.earthdata.nasa.gov/s3fs-public/imported/CSDAPReport0420.pdf.

Niroumand-Jadidi, M., Legleiter, C. J., and Bovolo, F. (2022). River bathymetry retrieval from Landsat-9 images based on neural networks and comparison to SuperDove and Sentinel-2. *IEEE J. Sel. Top. Appl. Earth Obs. Remote Sens.* 15, 5250–5260. doi:10.1109/jstars.2022.3187179

Pacheco, A., Horta, J., Loureiro, C., and Ferreira, Ó. (2015). Retrieval of nearshore bathymetry from Landsat 8 images: a tool for coastal monitoring in shallow waters. *Remote Sens. Environ.* 159, 102–116. doi:10.1016/j.rse.2014.12.004

Pahlevan, N., Mangin, A., Balasubramanian, S. V., Smith, B., Alikas, K., Arai, K., et al. (2021). ACIX-Aqua: a global assessment of atmospheric correction methods for Landsat-8 and Sentinel-2 over lakes, rivers, and coastal waters. *Remote Sens. Environ.* 258, 112366. doi:10.1016/J.RSE.2021.112366

Pahlevan, N., Balasubramanian, S., Begeman, C. C., O'Shea, R. E., Ashapure, A., Maciel, D. A., et al. (2024). A retrospective analysis of remote-sensing reflectance products in coastal and inland waters. *IEEE Geoscience Remote Sens. Lett.* 21, 1–5. doi:10.1109/lgrs.2024.3351328

Pahlevan, N., Chittimalli, S. K., Balasubramanian, S. V., and Vellucci, V. (2019). Sentinel-2/Landsat-8 product consistency and implications for monitoring aquatic systems. *Remote Sens. Environ.* 220, 19–29. doi:10.1016/J.RSE.2018.10.027

Pahlevan, N., Lee, Z., Wei, J., Schaaf, C. B., Schott, J. R., and Berk, A. (2014). On-orbit radiometric characterization of OLI (Landsat-8) for applications in aquatic remote sensing. *Remote Sens. Environ.* 154, 272–284. doi:10.1016/J.RSE.2014.08.001

Pahlevan, N., Sarkar, S., Franz, B. A., Balasubramanian, S. V., and He, J. (2017a). Sentinel-2 MultiSpectral Instrument (MSI) data processing for aquatic science applications: demonstrations and validations. *Remote Sens. Environ.* 201, 47–56. doi:10.1016/J.RSE.2017.08.033

Pahlevan, N., Schott, J. R., Franz, B. A., Zibordi, G., Markham, B., Bailey, S., et al. (2017b). Landsat 8 remote sensing reflectance (Rrs) products: evaluations, intercomparisons, and enhancements. *Remote Sens. Environ.* 190, 289–301. doi:10.1016/J.RSE.2016.12.030

Pahlevan, N., Smith, B., Alikas, K., Anstee, J., Barbosa, C., Binding, C., et al. (2022). Simultaneous retrieval of selected optical water quality indicators from Landsat-8, Sentinel-2, and Sentinel-3. *Remote Sens. Environ.* 270, 112860. doi:10.1016/J.RSE.2021.112860

Pahlevan, N., Smith, B., Schalles, J., Binding, C., Cao, Z., Ma, R., et al. (2020). Seamless retrievals of chlorophyll-a from Sentinel-2 (MSI) and Sentinel-3 (OLCI) in inland and coastal waters: a machine-learning approach. *Remote Sens. Environ.* 240, 111604. doi:10.1016/j.rse.2019.111604

Pitarch, J., and Vanhellemont, Q. (2021). The QAA-RGB: a universal three-band absorption and backscattering retrieval algorithm for high resolution satellite sensors. Development and implementation in ACOLITE. *Remote Sens. Environ.* 265, 112667. doi:10.1016/j.rse.2021.112667

Roy, P. S., Behera, M. D., and Srivastav, S. K. (2017). Satellite remote sensing: sensors, applications and techniques. *Proc. Natl. Acad. Sci. India Sect. A Phys. Sci.* 87, 465–472. doi:10.1007/s40010-017-0428-8

Saunier, S., and Cocevar, P. (2022). Technical note on quality assessment for SuperDove.

Semple, A. G., Tan, B., Lin, G., and Gary (2023). *SuperDove geometric quality assessment summary*. Greenbelt, MD.

Smith, B., Pahlevan, N., Schalles, J., Ruberg, S., Errera, R., Ma, R., et al. (2021). A chlorophyll-a algorithm for Landsat-8 based on mixture density networks. *Front. Remote Sens.* 1, 623678. doi:10.3389/frsen.2020.623678

Steinmetz, F., and Ramon, D. (2018). "Sentinel-2 MSI and Sentinel-3 OLCI consistent ocean colour products using POLYMER," in Remote sensing of the open and coastal Ocean and inland waters (Honolulu, HI: SPIE), 46–55.

Team, P. (2022). Planet Imagery Product Specifications February 2021. San Francisco, CA.

Team, P. L. (2023). Planet imagery product specifications December 2023. San Francisco, CA.

Team, S. M. E. (2022). Sentinel-2 annual performance report – year 2022. San Francisco, CA.

Tu, Y.-H., Johansen, K., Aragon, B., El Hajj, M. M., and McCabe, M. F. (2022). The radiometric accuracy of the 8-band multi-spectral surface reflectance from the planet SuperDove constellation. *Int. J. Appl. Earth Observation Geoinformation* 114, 103035. doi:10.1016/j.jag.2022.103035

USGS (2020). Commercial smallsat data acquisition program system characterization report for PlanetScope SuperDove instruments. U.S. Geological Survey. Available online at: https://www.earthdata.nasa.gov/s3fs-public/imported/CSDAPReport0420.pdf (Accessed July 24, 2025).

Vanhellemont, Q. (2019a). Daily metre-scale mapping of water turbidity using CubeSat imagery. *Opt. Express* 27, A1372–A1399. doi:10.1364/oe.27.0a1372

Vanhellemont, Q. (2019b). Adaptation of the dark spectrum fitting atmospheric correction for aquatic applications of the landsat and Sentinel-2 archives. *Remote Sens. Environ.* 225, 175–192. doi:10.1016/J.RSE.2019.03.010

Vanhellemont, Q. (2023). Evaluation of eight band SuperDove imagery for aquatic applications. *Opt. Express* 31, 13851–13874. doi:10.1364/oe.483418

Vanhellemont, Q., and Ruddick, K. (2014). Turbid wakes associated with offshore wind turbines observed with landsat 8. *Remote Sens. Environ.* 145, 105–115. doi:10.1016/J.RSE.2014.01.009

Vanhellemont, Q., and Ruddick, K. (2018). Atmospheric correction of metre-scale optical satellite data for inland and coastal water applications. *Remote Sens. Environ.* 216, 586–597. doi:10.1016/j.rse.2018.07.015

Wang, D., Ma, R., Xue, K., and Loiselle, S. A. (2019). The assessment of Landsat-8 OLI atmospheric correction algorithms for inland waters. *Remote Sens. (Basel)* 11, 169. doi:10.3390/rs11020169

Wang, M. (2010). IOCCG, "atmospheric correction for remotely-sensed ocean-colour products". Dartmouth, NS: Reports of the International Ocean-Colour Coordinating Group.

Warren, M. A., Simis, S. G. H., Martinez-Vicente, V., Poser, K., Bresciani, M., Alikas, K., et al. (2019). Assessment of atmospheric correction algorithms for the Sentinel-2A MultiSpectral imager over coastal and inland waters. *Remote Sens. Environ.* 225, 267–289. doi:10.1016/J.RSE.2019.03.018

Wei, J., Lee, Z., Garcia, R., Zoffoli, L., Armstrong, R. A., Shang, Z., et al. (2018). An assessment of Landsat-8 atmospheric correction schemes and remote sensing reflectance products in coral reefs and coastal turbid waters. *Remote Sens. Environ.* 215, 18–32. doi:10.1016/j.rse.2018.05.033

Zhang, X., Wang, L., Li, J., Han, W., Fan, R., and Wang, S. (2023). Satellite-derived sediment distribution mapping using ICESat-2 and SuperDove. *ISPRS J. Photogrammetry Remote Sens.* 202, 545–564. doi:10.1016/j.isprsjprs.2023.06.009

Zolfaghari, K., Pahlevan, N., Simis, S. G. H., O'Shea, R. E., and Duguay, C. R. (2023). Sensitivity of remotely sensed pigment concentration *via* mixture density networks (MDNs) to uncertainties from atmospheric correction. *J. Gt. Lakes. Res.* 49, 341–356. doi:10.1016/j.jglr.2022.12.010